The origin of felsic intrusions within the mantle section of the Samail ophiolite: Geochemical evidence for three distinct mixing and fractionation trends

Matthew Rioux[1,2*], Mathieu Benoit[3], Isma Amri[4], Georges Ceuleneer[3], Joshua M. Garber[5], Michael Searle[6], Kayla Leal[1]

[1] *Department of Earth Science, University of California, Santa Barbara, CA, 93106, USA*
[2] *Earth Research Institute, University of California, Santa Barbara, CA, 93106, USA*
[3] *Centre National de la Recherche Scientifique, Observatoire Midi-Pyrénées , 31400 Toulouse, France*
[4] *Faculté des Sciences, Département de Géologie, Université Abdelmalek Essaadi, Tétouan, Morocco.*
[5] *Department of Geosciences, The Pennsylvania State University, University Park, PA 16802, USA*
[6] *Department of Earth Sciences, University of Oxford, Oxford, OX1 3AN, UK*
[*] *corresponding author: rioux@eri.ucsb.edu*

Submitted manuscript

Published as:
Rioux, M., Benoit, M., Amri, I., Ceuleneer, G., Garber, J. M., Searle, M., and Leal, K., 2021, The origin of felsic intrusions within the mantle section of the Samail ophiolite: Geochemical evidence for three distinct mixing and fractionation trends, *Journal of Geophysical Research*, v. 126, e2020JB020760. https://doi.org/10.1029/2020JB020760.

Key Points:

- Felsic dikes and sills with epsilon Nd of -7.8 to +7.8 intruded the shallow mantle in the Samail ophiolite
- Combined whole rock major-element, trace-element, and isotopic data define three distinct mixing and fractionation trends
- Most dikes form by sediment and amphibolite melting on underthrust oceanic lithosphere at P ≤ 1.4 GPa and T ≥ 700–750 C

Abstract
An isotopically diverse suite of felsic dikes, sills, and plugs ($\varepsilon_{Nd}(t)$ = -7.8 to +7.8) intrude the uppermost mantle and lower crust in the Samail ophiolite in Oman and the United Arab Emirates (UAE). These features have been interpreted to represent amphibolite and metasediment melts from an underthrust sheet of oceanic lithosphere. As such, the intrusions provide a record of melting of oceanic crust and sediment at depth, with implications for mass transfer from the down-going plate in young, hot subduction settings. Several studies have used geochemical data to constrain the magmatic sources of the dikes; here we build on this previous work using integrated whole rock major-element, trace-element and Nd isotopic data from a more geographically extensive suite of dikes. New and existing data suggest the felsic intrusions preserved within mantle peridotites in the Oman portion of the ophiolite were generated by three distinct mixing and fractionation trends: 1. Three-component mixing between sediment melt, amphibolite melt and a mantle component; 2. Two component mixing between amphibolite and sediment melts, with little mantle contribution; and 3. Fractional crystallization of depleted, mantle derived magmas, likely related to the ophiolite V2 volcanic series. Combined geochemical and pseudosection modeling suggest that amphibolite melting occurred at $P \leq 1.4$ GPa (~40–45 km) and $T \geq$ 700–750 °C. Felsic intrusions in the mantle section in the UAE—including garnet-andalusite-cordierite leucogranites—follow similar mixing trends, but crystallized ~0.9–4.0 Ma after the Oman intrusions.

1. Introduction
The Samail (Oman-UAE) ophiolite exposes an extensive section of Late Cretaceous oceanic lithosphere. The ophiolite is dominated by ultramafic to mafic rocks, with the exception of small-volume tonalite and trondhjemite intrusions ("plagiogranites") in the upper crust [*Bailey*, 1981; *Lippard et al*., 1986] and a relatively sparse series of felsic sills, dikes, and plugs that intermittently intrude the uppermost mantle and lower crust along the length of the ophiolite [*Adachi and Miyashita*, 2003; *Amri et al*., 1996; *Amri et al*., 2007; *Haase et al*., 2015; *Lippard et al*., 1986; *Rollinson*, 2009; *Rollinson*, 2014a; 2015]. The upper-crustal tonalite and trondhjemite intrusions are typically exposed directly below, and intruding into, the base of the sheeted dike complex. They have depleted radiogenic isotope ratios ($\varepsilon_{Nd}(t)$ ~ +7–8) [*Amri et al*., 2007; *Godard et al*., 2006; *Haase et al*., 2015; *McCulloch et al*., 1981; *Rioux et al*., 2012; *Rioux et al*., 2013; *Tsuchiya et al*., 2013]—similar to modern mid-ocean ridges—and geochemical data indicate they are related to either the main phase of ophiolite crust formation at the ridge axis (Geotimes or V1) or the overlying volcanic sequence (Lasail/Alley or V2) [e.g., *Adachi and Miyashita*, 2003; *Haase et al*., 2016; *MacLeod and Yaouancq*, 2000; *Pallister and Hopson*, 1981]. These upper-crustal intrusions have been attributed to crystallization of residual felsic melts derived by fractionation of primitive gabbro [*Amri et al*., 1996; *Pallister and Hopson*, 1981] or on-axis anatexis of gabbros or sheeted dikes related to interaction of magmatic and hydrothermal systems [*France et al*., 2009; *Koepke et al*., 2004; *Nicolas et al*., 2008; *Rollinson*, 2009]. Similar rock types are observed at modern slow- and fast-spreading ridges [e.g., *Aldiss*, 1981; *Natland and Dick*, 2002; *Wilson et al*., 2006].

In contrast, the felsic intrusions into the upper mantle and lowermost crust of the ophiolite are geochemically and mineralogically distinct; they are commonly enriched in light rare earth elements (LREE) and typically have low Nd isotopic ratios ($\varepsilon_{Nd}(t)$ < 0; i.e., continent-like), although some have higher positive $\varepsilon_{Nd}(t)$ [*Amri et al*., 2007; *Briqueu et al*., 1991; *Cox et al*., 1999; *Haase et al*., 2015; *Lippard et al*., 1986; *Rioux et al*., 2013]. Some of the felsic intrusions in the northern section of the ophiolite within the UAE are more aluminous garnet-, andalusite-, and cordierite-bearing leucogranites. U-Pb zircon dating indicates that the dikes within the Oman portion of the ophiolite intruded toward the end of crustal growth [*Rioux et al*., 2013; *Rioux et al*., in review], suggesting they are related to ophiolite formation or emplacement, rather than later obduction onto the continental margin. Based on the geochemical and isotopic data, the intrusions have been interpreted to reflect melting of metasediment and amphibolite on the top of either underthrust oceanic lithosphere [*Boudier et al*., 1988; *Briqueu et al*., 1991] or a subducted slab [*Haase et al*., 2015; *Rioux et al*., 2013; *Rollinson*, 2009; *Rollinson*, 2014a; 2015; *Spencer et al*., 2017]. The dikes are therefore a valuable analogue for the melting of oceanic crust and sediment at intermediate pressures and temperatures, which may be an important mass transfer process in young, hot subduction settings [e.g., *Maunder et al*., 2020; *Nikolaeva et al*., 2008].

The geochemistry of the felsic intrusions has been the focus of several previous studies [*Amri et al*., 2007; *Briqueu et al*., 1991; *Cox et al*., 1999; *Haase et al*., 2015; *Rollinson*, 2009; *Rollinson*, 2014a; 2015; *Spencer et al*., 2017]. Here we present new whole-rock major-element, trace-element and Nd-isotopic data from intrusions from a broader geographic area than previous studies. Integration of the elemental and isotopic data and the greater geographic extent provides new insight into the source of the felsic intrusions.

2. Geologic setting

The Samail ophiolite, exposed in Oman and the UAE, is the largest and best studied ophiolite on Earth (Figure 1). It exposes a complete crustal and shallow mantle section, with a general stratigraphy of residual mantle harzburgite, layered gabbro, foliated gabbro, discontinuous upper-level varitextured gabbro and tonalite/trondhjemite (plagiogranite), basaltic sheeted dikes, and pillow basalts and lava flows [*Coleman and Hopson*, 1981; *Lippard et al*., 1986; *Nicolas et al*., 2000; *Pallister and Hopson*, 1981]. The volcanic sequence in the ophiolite has been divided into the lower Geotimes (V1) and upper Lasail/Alley (V2) series [*Alabaster et al*., 1982; *Ernewein et al*., 1988; *Lippard et al*., 1986; *Pearce et al*., 1981]. Limited sedimentation between the two series suggest that these eruptive events may have been contiguous, with little to no time lapse between them. The V1 series, which is interpreted to reflect the extrusive equivalent to the main portion of the intrusive crust, is chemically similar to mid-ocean ridge basalts (MORB) [*Ernewein et al*., 1988; *Godard et al*., 2006], although the lavas follow differentiation trends to lower TiO_2 and higher SiO_2, and are depleted in Cr, Nb, and Ta relative to typical MORB [*MacLeod et al*., 2013; *Pearce et al*., 1981]. The overlying V2 (Lasail and Alley) lavas are depleted in fluid-immobile incompatible trace elements (e.g., Nb, Ta, REE, Zr) and enriched in large ion lithophile elements (LILE), and have been interpreted to reflect formation in a nascent subduction zone setting [*Alabaster et al*., 1982; *Kusano et al*., 2017; *Pearce et al*., 1981]. Lavas in the upper portion of the V2 series have boninitic compositions [*Ishikawa et al*., 2002; *Kusano et al*., 2017]. A similar dichotomy between MORB and boninitic-andesitic magmatic compositions exists in the population of mafic dikes intruding the mantle section of the ophiolite [*Benoit et al*., 1999]. The two series occupy different portions of the ophiolite, with the MORB dikes increasing in abundance in the southeastern massifs [*Benoit et al*., 1996; *Ceuleneer et al*., 1996; *Python and Ceuleneer*, 2003]. Several studies have used field relations and geochemistry to also link intrusive plutonic rocks in the ophiolite crust to the V1 and V2 lavas [e.g., *Adachi and Miyashita*, 2003; *Haase et al*., 2016; *Tsuchiya et al*., 2013; *Usui and Yamazaki*, 2010], and we refer to these as the V1 and V2 plutonic series in this contribution.

The ophiolite is underlain by a metamorphic sole composed of metabasaltic and metasedimentary lithologies. The highest-grade rocks consist of garnet- and clinopyroxene-bearing amphibolites, which are exposed in a narrow 1–10 m thick layer in direct thrust contact with overlying, highly sheared harzburgite [*Cowan et al.*, 2014; *Ghent and Stout*, 1981; *Hacker and Mosenfelder*, 1996; *Searle and Cox*, 2002a; *Searle and Malpas*, 1980; 1982; *Soret et al.*, 2017]. Estimated peak pressures (*P*) and temperatures (*T*) of metamorphism for the highest-grade rocks are 770–900ºC and 1.0–1.3 GPa [*Cowan et al.*, 2014; *Gnos*, 1998; *Hacker and Mosenfelder*, 1996; *Soret et al.*, 2017]. These are sequentially underlain by lower grade amphibolite- and then greenschist-facies mafic and metasedimentary rocks, defining an inverted metamorphic gradient [*Garber et al.*, 2020; *Gnos*, 1998; *Searle and Malpas*, 1980; *Soret et al.*, 2017]. These sole units are in turn thrust over low-grade metasedimentary and metavolcanic rocks of the Haybi and Hawasina Formations, which are interpreted as deep-sea sediments, Permian to Triassic limestones, and alkali basaltic seamounts [*Searle*, 1985; *Searle et al.*, 1980]. In the UAE portion of the ophiolite, an out-of-sequence thrust sheet of granulite to upper amphibolite metasedimentary and minor metabasaltic rocks is preserved within the mantle section at Bani Hamid, with peak *P-T* conditions of 850 ± 60 ºC and 0.63 ± 0.05 GPa [*Searle et al.*, 2015].

The felsic intrusions that are the focus of this study typically occur as ~1–10 m thick dikes, plugs, and sills that intrude the upper mantle and lowermost crust of the Samail ophiolite, although some intrusions are thicker (e.g., Bahla); for simplicity, we henceforth refer to these intrusions as "felsic mantle dikes". The dikes are found intermittently along the entire length of the ophiolite (Figure 1). Where present, they often occur in clusters or swarms, but individual swarms occur tens of kilometers apart, with only a few dike localities in each massif. The dikes are generally classified as diorites, tonalites, trondhjemites, and granites with 65–84 wt. % SiO_2. In addition to their unique field context and major-element expression, the dikes are isotopically distinct from the rest of the ophiolite. The V1 and V2 magmatic series in the ophiolite have $\varepsilon_{Nd}(t) \approx +7–8$, similar to modern ridges [*Amri et al.*, 2007; *Godard et al.*, 2006; *Haase et al.*, 2015; *McCulloch et al.*, 1981; *Rioux et al.*, 2012; *Rioux et al.*, 2013; *Tsuchiya et al.*, 2013], although whole rock data from boninitic lavas in the upper part of the V2 series have lower values of $\varepsilon_{Nd}(t)$ = +0.88 to +5.69 [*Kusano et al.*, 2017]. In contrast, published data from the felsic mantle dikes in Oman and the UAE have $\varepsilon_{Nd}(t)$ = -7.8 to +7.8, typically with $\varepsilon_{Nd}(t) < 0$ [*Amri et al.*, 2007; *Briqueu et al.*, 1991; *Cox et al.*, 1999; *Haase et al.*, 2015; *Rioux et al.*, 2013; *Rioux et al.*, in review].

3. Previous work

Several previous studies have addressed the origin of the felsic mantle dikes. The dikes were first identified and mapped as small biotite granite intrusions into the upper mantle and lowermost crust in the Haylayn and Wuqbah massifs [*Browning and Smewing*, 1981; *Lippard et al.*, 1986]. Geochemical analyses on two dikes from Oman and the UAE showed that the dikes are enriched in LREE and one dike yielded a low $\varepsilon_{Nd}(t)$ = -4.1, suggesting a source with a time-integrated LREE enrichment. Based on the geochemical and isotope data, and a K-Ar date from the UAE dike of 85 ± 3 Ma, these authors interpreted the dikes to reflect melting of continental material during obduction of the ophiolite over the Arabian margin. Using the same data, Pearce et al. [1989] similarly concluded that the dikes were related to melting of turbidite deposits on the Arabian continental rise during initial obduction.

To further constrain the origin of the felsic mantle dikes, Briqueu et al. [1991] carried out whole rock geochemical and Pb, Nd, and Sr isotopic analyses of i) felsic mantle dikes from the UAE and ii) metamorphic rocks from the Asimah-Masafi metamorphic sole locality and Bani Hamid thrust sheet. They found that the isotopic composition of the dikes was intermediate between a mantle source and more enriched, continental values. Based on these data, they argued that the dikes formed by melting of amphibolite and metasediments in the metamorphic sole of the ophiolite, during initial thrusting of the ophiolite over adjacent crust, with the residual heat of the ophiolite mantle acting as the heat source for sole metamorphism and melting. This model mirrored the conclusions of Boudier et al. [1988], who discussed the link between felsic mantle dikes and mantle shear zones. In a more limited study, Peters and Kamber [1994] presented geochemical data from the felsic dikes in the UAE. Based on comparisons to the quartz diorite to tonalite suite in the ophiolite crust, they argued that the dikes could reflect either extreme fractionation of mantle derived magmas or hydrous partial melting of the ophiolite crust or mantle, with the enriched isotopic compositions attributed to addition of a fluid component derived from the metamorphic sole.

Cox et al. [1999] carried out a detailed major element, trace element, and isotopic study of felsic intrusions throughout the UAE. Their data supported the conclusion of Briqueu et al. [1991] that the dikes reflect mixing between metabasalt and metasedimentary partial melts. They similarly argued that the metasedimentary source had a composition similar to the Bani Hamid granulites and the metabasaltic source was compositionally similar to amphibolites preserved in the metamorphic sole (or equivalent un-metamorphosed volcanic units in the Haybi complex). Using whole-rock elemental and isotopic data, they argued that the dikes formed through both dehydration and fluid saturated melting at pressures of 0.3–0.5 GPa. Cox et al. [1999] attributed formation of the dikes to metamorphism and melting at the top of a subducting slab.

In the Oman portion of the ophiolite, Amri et al. [2007] reported major-element, trace-element, and Nd and Sr isotopic data for numerous felsic mantle dikes, ultimately attributing their petrogenesis to mixing between a depleted mantle source, a hydrothermal component, and potentially a component of terrigenous sediment. Four recent studies have addressed the origin of the Oman dikes in more detail. Haase et al. [2015] focused on the cluster of intrusions in the southern Haylayn massif, previously studied by Browning and Smewing [1981] and Lippard et al. [1986]. They noted mixing trends in major-element, trace-element, and Hf isotopic data versus MgO, and argued for two-component mixing between sediment melts derived from the top of a subducting slab and basalts formed by partial melting of the overlying mantle wedge. Rollinson [2014a; 2015] presented additional whole rock geochemical data from felsic intrusions from the same area in the Haylayn massif, a cluster of intrusions in the Fizh massif, and intrusions in the UAE portion of the ophiolite. Focusing on dikes with the least fractionated compositions, he suggested that xenocrystic calcic plagioclase, small mafic inclusions within the dikes, and major- and trace-element variations were consistent with a component of melted amphibolite. Rollinson [2014a; 2015] concluded that the dikes formed by three-component mixing between partial melts derived from amphibolite to granulite facies meta-basalts in a subducted slab, partial melts of subducted sediment from the top of the slab, and assimilation of orthopyroxene and amphibole from harzburgites during accent of the slab melts through the mantle wedge. In a complementary study, Spencer et al. [2017] carried out oxygen isotope analyses on felsic mantle dikes in Oman and the UAE. The dikes recorded elevated zircon $\delta^{18}O$ = 14–18 ‰, which the authors attributed to melting of pelitic or siliceous sediment on the top of a subducted plate.

In a companion study to this manuscript [*Rioux et al*., in review], we present new high-precision U-Pb dating, which constrains the timing of dike intrusion relative to formation of the ophiolite crust, as well as age variations in the felsic mantle dikes along the length of the ophiolite. Our previous work has shown that gabbros related to the V1 volcanic series—the main phase of crustal growth in the ophiolite—yield zircon dates of 96.1–95.6 Ma [*Rioux et al*., 2012; *Rioux et al*., 2016], indicating rapid crustal growth. Plutonic rocks associated with the V2 magmatic series yield slightly younger dates of 95.6–95.2 Ma [*Rioux et al*., 2013; *Rioux et al*., in review]. The rapid formation of the crust is consistent with ophiolite formation along an NNW-SSE oriented spreading ridge (present geographical reference frame), parallel to the trend of the sheeted dikes. Our new U-Pb zircon analyses from four felsic mantle dikes from Oman yielded dates from 95.2–95.0 Ma, in agreement with our previous results from two additional samples (95.2–95.1 Ma) [*Rioux et al*., 2013], indicating intrusion at the end of crustal growth [*Rioux et al*., in review]. A single dike from the Sarami massif yielded an older date of 95.478 ±0.032 Ma (discussed below). In contrast to the near synchronous dates throughout Oman, five dated dikes from the UAE yielded significantly younger and highly variable dates from 94.1–91.0 Ma [*Rioux et al*., in review]. The distinct U-Pb dates from the Oman and UAE dikes indicate that the two intrusive series crystallized ~0.9–4.0 million years apart. To better constrain the origin of the felsic dikes and assess their chemical heterogeneity along the length of the ophiolite, we here report whole rock major- and trace-element data for the dated dikes from Oman, two of the dated dikes from the UAE, and a larger geochemical dataset from undated intrusions in Oman

4. Samples

The studied samples come from intrusions into the mantle and lowermost crust along the length of the ophiolite (Figure 1 and Table 1). Five of the samples were collected by Rioux and Garber in Oman. Three are tonalite to trondhjemite intrusions into the mantle section (13211M02, 13215M08, 13221M05) and one is a tonalite intrusion into layered gabbros just above the crust-mantle boundary (13219M03)—these intrusions are from the Bahla, Fizh, Wadi Tayin, and Haylayn massifs, respectively. These samples have yielded Th-corrected $^{206}Pb/^{238}U$ dates of 95.201 ± 0.032 to 94.95 ± 0.10 Ma, with $\varepsilon_{Nd}(t)$ = –1.63 to –5.05 (Table 2) [*Rioux et al*., in review]. The fifth sample from Oman, a tonalite that intrudes mantle harzburgite in the Sarami massif (13217M01), yielded a slightly older date of 95.478 ± 0.032 Ma and higher $\varepsilon_{Nd}(t)$ = 7.35 [*Rioux et al*., in review]. Two additional samples were collected by Searle in the UAE. MS13-1 is a garnet, muscovite, biotite leucogranite from a swarm of felsic intrusions into peridotite in Wadi Hulw bin Sulayman. MS13-5 comes from a series of intrusions at Ra's Dadnah, which include two distinct compositions: a first suite of biotite-hornblende to biotite granite intrusions and a nearby suite of peraluminous leucogranites containing andalusite, cordierite, garnet, biotite, and tourmaline. MS13-5 is a tourmaline-garnet leucogranite from the latter suite. These samples yielded Th-corrected $^{206}Pb/^{238}U$ dates of 94.119 ± 0.057 Ma (MS13-1) and 92.361 ± 0.026 Ma (MS13-5), with $\varepsilon_{Nd}(t)$ = –4.96 and –4.63, respectively.

All remaining dike samples were collected by Amri, Ceuleneer, and Benoit. Sm-Nd and Rb-Sr isotopic data and some whole-rock geochemical data for these samples were previously discussed by Amri et al. [2007]; however, the full datasets were not reported in that contribution and are reported here (Table 3). The analyzed samples include granite, tonalite, and quartz diorite intrusions into mantle peridotite and a single tonalite intrusion into lower crustal layered gabbros (94M375). An intrusion adjacent to sample 94M375 previously yielded a U-Pb zircon date of 95.063 ± 0.062 Ma [*Rioux et al*., 2013].

Finally, to better constrain the composition of underthrust sediment, we also present trace element data from a single garnet- and muscovite-rich metasediment (13222M06) collected by Rioux and Garber from ~12 m below the Samail Thrust at the Green Pool sole locality in the Wadi Tayin massif. Nd isotope and major-element data have previously been reported by Rioux et al. [2016] and Garber et al. [2020], respectively. The metasediment is composed of quartz + white-mica + biotite + plagioclase + garnet + ilmenite + magnetite, and occurs as a m-scale layer within a section of amphibolite—see Garber et al. [2020] for a detailed discussion of the petrogenesis and field relations.

5. Methods and Results

Geochemical data were analyzed at the Washington State University GeoAnalytical Lab; the Centre de Recherches Pétrographiques et Geochimiques (CRPG) at the Université de Lorraine; the Observatoire Midi-Pyrénées (OMP), Unités Mixtes de Recherche (UMR) 556, Toulouse; and Institut Universitaire Europeen de la Mer (IUEM), UMR6538, Plouzané. For the Washington State analyses (Table 2), major- and minor-elements were analyzed on fused beads by x-ray fluorescence, following the procedures of Johnson et al. [1999]. Trace element analyses were carried out by inductively coupled plasma-mass spectrometry (ICP-MS) using a combined fusion-acid digestion method, following the procedures of Knaack et al. [1994]. Estimates of analytical precision are provided in Table 2, based on comparison of repeat analyses of 250 unknowns for the XRF data [*Kelly*, 2018] and 50 analyses of the AGV-1 standard over 5 years for the ICP-MS data [*Steenberg et al*., 2017]. The accuracy of Washington State XRF analyses has been estimated as the relative percent difference between regressions of measured versus reported values for certified reference materials, with deviations of 0.03% (Na_2O) to 4.1% (TiO_2), with an average of 1.6% for major elements, and an average deviation of 3.1% for trace elements, with elevated values for Zr (7.7%) and Y (8.5%) [*Kelly*, 2018]. The accuracy of Washington State ICP-MS analyses has been estimated from the relative percent difference from consensus values of 100 analyses of certified reference materials over 5 years; percent differences range from 1.6–9.0%, with values ≤3.1% for all elements except Sm, Eu, Tb, Dy, Ho, and Er (4.8–9.0 %) [*Steenberg et al*., 2017]. For the OMP-CRPG-IUEM data (Table 3), whole rock major and minor elements were analyzed on fused glass beads by XRF at CRPG. Trace element analyses were again carried out by ICP-MS using a combined lithium borate fusion-acid digestion procedure at UMR5563-OMP; analytical procedures and accuracy are discussed in Aries et al., [2000] and Braun et al. [1998]. Nd and Sr isotopes were measured following the procedure described in Amri et al., [2007] at UMR6538, IUEM, Plouzané.

The major and trace element data are summarized in Figures 2–7, Tables 2 and 3 and Supplemental Figure S1. The analyzed dikes have 71.3–78.1 wt. % SiO_2, with the exception of a single quartz diorite with 57.4 wt. % SiO_2 (98T31C, Wadi Tayin massif, Table 3). Compared to the V1 and V2 plutonic rocks from the ophiolite crust, dikes from the Wadi Tayin, Bahla, northern Haylayn, Sarami, and Fizh massifs in the Oman portion of the ophiolite have high K_2O (up to 5.5 wt. %; Figures 2e and 3f), and are generally peraluminous (Figure 2c; Other Oman symbols), implying elevated Al_2O_3 relative to felspar stoichiometry; the single low SiO_2 quartz diorite intrusion is metaluminous. Chondrite-normalized REE patterns from the intrusions at these localities range from U- and V-shaped to LREE enriched with flat heavy REE (HREE), with the exception of 13217M01, which has an LREE depleted pattern (Figure 4c). The intrusions are depleted in Ti and enriched in Rb, Ba, K, Pb, Th, and U—and to a lesser extent Ta and Nb—relative to the V1 and V2 volcanic rocks from the ophiolite (Figure 4).

In contrast to the other Oman dike localities, published data [*Haase et al*., 2015; *Rollinson*, 2014a; 2015] and a single datum from this study from the Wadi Hajr and Wadi Hemli intrusions in the southern Haylayn massif include both metaluminous and peraluminous compositions, have higher MgO, and have lower K_2O on average (“Haylayn” symbols in Figures 2 and 3). These intrusions generally have LREE-enriched and relatively flat HREE chondrite-normalized patterns (Figure 4b); in all of the Oman dike samples, only a few rare samples show significant HREE depletion. Much of the previous research on the Oman dikes have focused on the Wadi Hajr and Wadi Hemli intrusions [*Haase et al*., 2015; *Rollinson*, 2014a; 2015], although Rollinson [2015] also studied dikes from a locality in the Fizh massif.

In the UAE, published data [*Cox et al*., 1999; *Rollinson*, 2015] and the two samples from this study overlap the non-Haylayn Oman dikes. The UAE data primarily plot within the peraluminous field, with a smaller number of metaluminous and peralkaline samples (Figure 2d), and are elevated in K_2O, relative to the V1 and V2 plutonic rocks (Figures 2f and 3f). Data from Ra's Dibba and Ra's Dadnah extend to more peraluminous compositions than the Oman data, which is consistent with the observed presence of Al-rich minerals in these intrusions, including garnet, cordierite, and andalusite [*Cox et al*., 1999]. Excluding Al Bithnah, REE patterns range from LREE enriched with flat HREE to nearly flat REE patterns with extreme negative Eu anomalies (Figure 4d; discussed in detail by Rollinson, 2015). In contrast, samples from Al Bithnah have steep LREE enriched and HREE depleted patterns, small positive or no Eu anomalies, and higher K_2O (Figures 2f and 4d).

The sediment (13222M06) from the Wadi Tayin metamorphic sole locality is characterized by LREE enrichment with flat HREE; Rb, Ba, Th, U, K, Ta, and Nb enrichment relative to MORB and the V1 lavas in the ophiolite; and Nb and Ta depletion relative to other incompatible trace elements (Figure 4a).

The Nd and Sr isotopic data for the felsic mantle dike samples in this study have previously been discussed by Rioux et al. [in review] and Amri et al. [2007] (Tables 2 and 3). Whole rock isotopic values from the samples range from $\varepsilon_{Nd}(t) = -5.8$ to $+4.1$, with two higher datum of $\varepsilon_{Nd}(t) = +7.4$ and $+7.8$ (Figure 5), and $^{87}Sr/^{86}Sr_{int.} = 0.703763$ to 0.709404. The Nd and Sr data are correlated, with high ε_{Nd} corresponding to lower $^{87}Sr/^{86}Sr$. The sole metasediment has an $\varepsilon_{Nd}(t) = -8.35$ [*Rioux et al*., 2016].

6. Discussion

6.1 Origin of the felsic mantle dikes in the Oman portion of the ophiolite

Given the significant age differences between the felsic mantle dikes in the southern (Oman) and northernmost (UAE) portions of the ophiolite, we discuss their origin separately. We start with the Oman dikes, which intruded at the end of crystallization of the oceanic crust of the ophiolite. Figures 5 and 6 illustrate the geochemical trends discussed below, with plot symbols grouped and colored based on the distribution of dike compositions on plots of MgO or SiO_2 versus $\varepsilon_{Nd}(t)$ (Figure 5a, b). On these plots, the data from the Oman felsic mantle dikes define two orthogonal trends. Data from the southern Haylayn massif define a near-horizontal trend of variable MgO with nearly constant $\varepsilon_{Nd}(t) = -4$ to -6 (red symbols). REE patterns from these samples are generally LREE enriched with flat HREE (Figure 6f), similar to metasedimentary sample 13222M06 from the metamorphic sole of the ophiolite (solid black line, Figure 6f). These major- and trace-element trends and the REE patterns can be explained by mixing or reaction between a low MgO, low ε_{Nd} sediment (± amphibolite) partial melt and a high MgO-Ni mantle component, consistent with the Haase et al. [2015] and Rollinson [2014a; 2015] studies, which focused on this area. Haase et al. [2015] argued that the mantle component is mantle derived basaltic melt—consistent with the increase in TiO_2 concentration with increasing mantle component (Figure 5d)—while Rollinson [2014a; 2015] suggests that interaction with mantle harzburgite is a more efficient way to increase the MgO and compatible trace element (e.g., Ni, Cr) concentrations.

Data from felsic mantle dikes from most other areas in Oman define a perpendicular trend to the Haylayn mixing array (green symbols), with variable $\varepsilon_{Nd}(t)$ at low MgO (<1 wt. %), low Ni (<18 ppm), and high SiO_2 (>70 wt. %) (Figures 5a, b, c). At $\varepsilon_{Nd}(t) > -2$, the REE patterns from the dikes are predominantly U- and V-shaped (Figures 6b-d); dikes with $\varepsilon_{Nd}(t) < -2$ have primarily LREE enriched patterns, with a few V-shaped patterns (Figure 6e, f). The U-shaped patterns match the expected REE pattern for partial melts derived from MORB metamorphosed at amphibolite facies conditions (black dashed line, Figures 6b–d), due to preferential partitioning of the MREE into amphibole (± clinopyroxene). We hypothesize that the more pronounced V-shaped patterns in some samples (Figure 6d) may result from variations in amphibole partition coefficients or the impact of additional residual phases during melting, such as titanite (Supplemental Text S1). In this context, we suggest that the low MgO trend (green symbols) is a result of partial melting of underthrust sediment and metabasalt; the low $\varepsilon_{Nd}(t)$ end member (blue symbols) has the highest proportion of sediment-derived partial melts, while the higher ε_{Nd} samples (green symbols) are increasingly dominated by partial melts derived from amphibolite- to granulite-facies metabasalts. The correlation between ε_{Nd} and REE patterns cannot be explained by fractional crystallization of amphibole (or any phase) from the felsic dikes, as crystallization does not change isotopic ratios.

The distinct mantle mixing (red symbols) and amphibolite melting (green symbols) trends are apparent in other major- and trace-element data (Figures 3 and 5). For example, the two datasets display distinct slopes on major-element variation diagrams (e.g., Figure 5d). The high SiO_2, low MgO, and other major-element trends are consistent with the observed composition of amphibolite melts from experimental studies at pressures and temperatures similar to those observed in the metamorphic sole of the ophiolite (Figures 3 and 5d) [*Rapp et al.*, 1991; *Rushmer*, 1991; *Zhang et al.*, 2013].

Patiño Douce [1999] developed major-element discrimination diagrams for melts derived from meta-sediments versus meta-basalts, based on a compilation of experimental data. For the Oman mantle dikes, the low MgO, low ε_{Nd} sediment-rich end member compositions (blue symbols) plot parallel to the trend of melts derived from felsic metapelites, while the dikes with higher ε_{Nd}—and a larger amphibolite component (green symbols)—are generally transitional between the compositions of meta-sediment and amphibolite melts (Figure 5e). The Haylayn dikes plot within the amphibolite melt field on this diagram, but this likely reflects mixing with a mantle component; the compositions of mantle-derived magmas overlap the amphibolite melt field, as seen in the V1 and V2 data.

Outside of the amphibolite melting and mantle mixing trends, there are almost no dikes with elevated ε_{Nd} (–2 to 4) and high MgO (>2 wt. %), high Ni (>20 ppm) or low SiO_2 (<70 wt. %) (i.e., the center of Figures 5a–c). The dearth of such data supports our conclusion that the U- and V-shaped REE patterns observed in the amphibolite melting trend reflect REE partitioning during partial melting of amphibolite, rather than amphibole fractionation from compositions along a more positive ε_{Nd} (–2 to 4) extension of the Haylayn mantle-sediment mixing trend (red diamonds). Differentiation of compositions from the Haylayn trend would likely generate dikes along a constant ε_{Nd} chord (–2 to 4) with intermediate MgO, SiO_2, and Ni concentrations—due to crystallization of mafic phases from the MgO-rich compositions—but such compositions are not observed. It is possible that the data reflect a sampling bias, since we largely focused on felsic, MgO poor rocks, and the separation of the two mixing trends could be further tested by additional sampling. The two distinct trends also suggest that the Haylayn swarm is unique in incorporating a significant mantle component. The one exception to this is a single sample from the Wadi Tayin massif [98T31C; *Amri et al.*, 2007], which plots within the Haylayn mixing trend (square, red symbol, Figure 5a); two other samples from the same locality plot within the amphibolite melting trend, suggesting significant heterogeneities within dike swarms over small length scales (10s to 100s of meters). Beyond the concentration of high MgO, low ε_{Nd} dikes in the southern Haylayn massif, there are no obvious geographic trends in the isotopic data (Figure 5j).

The low ε_{Nd}, low MgO dikes (blue symbols) plot at the confluence of the amphibolite melting and mantle mixing trends and therefore are expected to represent the most sediment-melt rich end members. In our prior work, we showed that metasediment from the Wadi Tayin massif—which we report whole rock geochemical data for here—has $\varepsilon_{Nd}(t)$ = -8.4 [*Rioux et al.*, 2016; 13222M06], suggesting that some sediments thrust below the ophiolite had even lower ε_{Nd} than observed in the mantle dikes. Based on this datum, it is possible that even the dikes with the lowest MgO and $\varepsilon_{Nd}(t)$ (blue symbols) are a mix of amphibolite with higher $\varepsilon_{Nd}(t)$ and sediment melt, rather than pure sediment melts. This conclusion is consistent with Rollinson [2015], who argued that small mafic inclusions and potentially xenocrystic high anorthite cores in the Haylayn dikes are related to amphibolite melting, and successfully modeled the REE patterns and other trace element abundances of the southern Haylayn intrusions (red symbols) as a mix of amphibolite and sediment partial melts (black dashed line, Figure 6f), combined with a mantle component. In contrast, Spencer et al. [2017] argued that zircon and whole-rock oxygen isotope data from the southern Haylayn dikes are best explained by pure sediment melting, with no mantle derived (or amphibolite) component. Our data do not preclude this possibility for some of the lowest MgO and $\varepsilon_{Nd}(t)$ samples (blue symbols); however, it is clear from the Ni and MgO data that many of the higher MgO Haylayn dikes contain a mantle component, and similarly, we consider it likely that some or all of the lowest MgO and $\varepsilon_{Nd}(t)$ samples (blue symbols) represent a mix of amphibolite and sediment melts, rather than pure sediment melts.

While the blue datapoints likely have the greatest sediment component, one of these dikes has a V-shaped REE pattern, suggesting the REE budget was dominated by amphibolite derived melts. Amphibolites from the metamorphic sole of the ophiolite have variable ε_{Nd} = +3.9 to +7.1 [*Cox et al.*, 1999; *Rioux et al.*, 2016], and a leucocratic pod within amphibolite from the Wadi Tayin sole locality had ε_{Nd} = –7.0 [*Rioux et al.*, 2013]. The low ε_{Nd} of some amphibolites could reflect either isotopic heterogeneity of the protolith basalt, or more likely, incorporation of a significant sedimentary component into the amphibolites. The low $\varepsilon_{Nd}(t)$ dike with a V-shaped REE pattern may therefore include a large component of melt derived from low $\varepsilon_{Nd}(t)$ amphibolite. Alternately, the V-shaped pattern could reflect variable REE patterns from sediment melts; however, we consider this to be less likely, given that most of the low ε_{Nd} dikes (i.e., sediment-rich) have LREE enriched patterns (Figure 6f, red and blue). In addition, while sediment derived Himalayan leucogranites do show a range of REE patterns [*Guo and Wilson*, 2012], it is notable that they do not include the type of V-shaped patterns observed in the Samail ophiolite.

Two final dikes have low MgO and high $\varepsilon_{Nd}(t)$ = +7.4–7.8 (yellow symbols), overlapping the range of $\varepsilon_{Nd}(t)$ observed within the V1 and V2 magmatic series that form the ophiolite crust (Figure 5a). These dikes plot at the intersection of the amphibolite melting trend (green symbols) described above, and the differentiation trends for the V1 and V2 magmatic series. One of these dikes (13217M01; $\varepsilon_{Nd}(t)$ = +7.4) from just below the crust-mantle transition in the Sarami massif has an LREE depleted REE pattern, which is distinct from the U-shaped REE patterns of the amphibolite melting trend, but similar to the REE patterns of the V2 volcanic series (labeled sample in Figures 4a, c and 6a; higher MgO yellow data point in Figure 5). This dike has a similar incompatible trace element signature to the V2 lavas, including Nb, Ta, and Th depletions and Pb and Sr peaks (Figure 4a). We therefore consider it most likely that this felsic dike formed by extensive differentiation of magmas related to the V2 series within the uppermost mantle. Interestingly, there is an offset in dates between the LREE depleted dike (13217M01) and the four dated LREE enriched mantle dikes [*Rioux et al.*, in review]; the LREE depleted dike yielded a weighted mean $^{206}Pb/^{238}U$ date of 95.478 ± 0.032 Ma, compared to younger $^{206}Pb/^{238}U$ dates of 95.201 ± 0.032 to 94.95 ± 0.10 Ma for the other mantle dikes. The older date overlaps with the timing of crustal plutonic rocks related to V2 magmatism [*Rioux et al.*, in review]. The data therefore suggest two distinct generations of felsic mantle intrusions, with an earlier set related to V2 magmatism and a later series linked to melting of underthrust amphibolite and metasediment.

In contrast, the second high $\varepsilon_{Nd}(t)$ dike (94M375; $\varepsilon_{Nd}(t) = +7.8$) was sampled just above the crust-mantle transition in the Samail massif, and has a slightly enriched LREE and relatively flat HREE pattern (labeled sample in Figures 4c and 6a; lower MgO yellow datapoint in Figure 5) [*Amri et al.*, 2007]. Rioux et al. [2013] studied an intrusion from the same swarm ~100 m from this sample, which yielded $\varepsilon_{Nd}(t) = +6.9$ and a $^{206}Pb/^{238}U$ date of 95.063 ± 0.062 Ma (9127M01), but we do not have trace-element data for the dated sample. The age of sample 9127M01 overlaps with the timing of the low $\varepsilon_{Nd}(t)$ mantle dikes and is distinctly younger than the age of the potentially V2 related intrusion discussed in the preceding paragraph. We therefore hypothesize that samples 94M375 and 9127M01, which have $\varepsilon_{Nd} = +6.9–7.8$, represent a high ε_{Nd} end member of primarily amphibolite melts. The major element data from 94M375 plot within the amphibolite melt field on the Patiño Douce [1999] major-element discrimination diagram, consistent with this hypothesis; however, the REE data for 94M375 lack the U-shape pattern associated with amphibolite melting. This could be due to differentiation or a different, more amphibole-poor or garnet-rich source composition. We note that the sample has an extreme Zr depletion (lowest Zr trough in Figure 4c) and a positive Eu anomaly, which could reflect zircon fractionation and plagioclase accumulation; however, simple geochemical models of these processes do not reproduce the observed REE pattern. Direct measurements of the REE in plagioclase, zircon and other trace minerals in the sample are required to more robustly test whether the observed REE pattern is related to differentiation or a different source lithology (e.g., more modal garnet).

The distinct melting and fractionation trends are best defined by major-element, minor element, and REE trends; however, incompatible trace element ratios provide additional insight into the source compositions and melting processes. The analyzed sole metasediment (13222M06) has a composition similar to Global Subducting Sediment (GLOSS) [*Plank and Langmuir*, 1998] and is enriched in Rb, Ba, Th, U, Nb, Ta, Pb, and the LREE relative to V1 volcanic compositions (Figures 4 and 7), providing constraints on the possible composition of the metasediment end member. Whole rock trace element compositions of sole amphibolites are intermediate between V1 and metasediment compositions, with variable enrichments in Rb, Ba, Pb, and Nb, which have been attributed to addition of these elements by slab fluids [*Ishikawa et al.*, 2005]; U and Th data were not published for the sole amphibolites. The more amphibolite-rich dikes in the Samail ophiolite are characterized by lower Th and U concentrations (Figure 7), as expected given the large compositional differences between likely sediment and amphibolite protoliths. The low Th of the amphibolite-rich melts leads to a general trend of decreasing Th/Yb with increasing amphibolite component (Figure 5g).

Previous work has also demonstrated that amphibolite melts are generally characterized by elevated Zr/Sm and low Nb/Ta [*Foley et al.*, 2002]. The inferred amphibolite-rich dikes (green data points) show a broad trend to higher Zr/Sm (Figure 5h), consistent with this observation;

scatter in the trend likely reflects heterogeneity in the slab sediment composition. The low Zr/Sm of the non-V2 related high ε_{Nd} dike (yellow plot symbol)—which we argue has the lowest sediment contribution—is likely related to zircon fractionation, as discussed above. While Foley et al. [2002] also used Nb/Ta to fingerprint amphibolite versus eclogite melting, this is a poor discriminant between amphibolite and lower pressure metasediment melts, as the range of sediment derived leucogranites from the Himalaya [*Guo and Wilson*, 2012] overlap the predicted range of Nb/Ta of amphibolite melts and no clear trend is seem in the felsic dike data.

Finally, sediment-derived Himalayan leucogranites are characterized by low Ce/Pb (< 2) [*Guo and Wilson*, 2012] and the analyzed sole meta sediment has a lower Ce/Pb (Ce/Pb = 5.2) than most sole amphibolites (Ce/Yb = 3.5–43.3) [*Ishikawa et al*., 2005] and V1 volcanic rocks (3.0–83.2) [*Godard et al*., 2003; *Godard et al*., 2006], suggesting this may be a useful ratio to discriminate between amphibolite and metasedimentary sources within the mantle dikes. However, there is no systematic offset in Ce/Pb between sediment-rich and amphibolite-rich dikes (Figure 5i; Ce/Pb overlap for blue and green plot symbols). This may reflect Pb addition in a fluid phase during amphibolite melting, although this is ambiguous as we do not observe a clear trend to lower Th/U (fluid immobile/fluid mobile) for amphibolite-rich dikes and Ishikawa et al. [2005] found only limited Pb enrichment from slab fluids in sole amphibolites.

In summary, our analyses suggest the felsic dikes that intrude the upper mantle and lowermost crust along the length of the ophiolite formed as a result of three distinct fractionation and mixing processes: 1. Dikes with low MgO (<1 wt. %), low Ni, high SiO_2, and ε_{Nd} = –6 to +4 (green and blue symbols) likely represent two component mixing between partial melts from amphibolite- to granulite-facies metasedimentary and meta-basaltic sources that were underthrust or subducted below the ophiolite, with an increasing component of metabasaltic melts at higher ε_{Nd}. 2. Dikes with low ε_{Nd} = –6 to –4, but higher MgO (>1 wt. %), higher Ni, and lower SiO_2 (red symbols) likely reflect mixing between combined meta-basaltic/meta-sedimentary melts and a mantle component consisting of either mantle derived basalts [*Haase et al*., 2015] or reaction with mantle harzburgite [*Rollinson*, 2015]. And 3. a single dike with low MgO, high ε_{Nd} = +7.4 and an LREE depleted rare earth element pattern may have formed by extensive differentiation of V2 magmas within the upper mantle.

6.2 Origin of the felsic mantle dikes in the UAE portion of the ophiolite

The felsic dikes within the mantle section in the UAE are ~0.9–4.0 Ma younger than the similar intrusions within the Oman section [*Rioux et al*., in review]. Cox et al. [1999] used isotopic and geochemical data to argue that the UAE dikes range from pure metasediment partial melts to mixtures of metasediment and meta-basaltic partial melts. Rollinson [2015] grouped the Oman and UAE dikes together in deriving his three-component mixing model. The plots presented herein are generally consistent with the conclusions of Cox et al. [1999]; most of the UAE dikes—from Ra's Dadnah, Ra's Dibba, Wadi Hulw bin Sulayman, and Wadi Zikt—plot along the amphibolite mixing trend, suggesting they represent a mix of metasedimentary and metabasaltic melts formed at amphibolite- to granulite-facies (Figure 5). A single dike analyzed by Cox et al. [1999] from the center of the Ra's Dadnah composite intrusion plots along the mantle mixing trend, consistent with assimilation of orthopyroxene and amphibole from mantle harzburgites [*Rollinson*, 2015] or mixing with mantle derived basalt [*Haase et al*., 2015]. These data suggest that – although there are significant age differences – the UAE felsic dikes broadly record the same melting, mixing, and fractionation processes as the Oman dikes.

6.3 Depth of melting

An important observation made by both Haase et al. [2015] and Rollinson [2015] is that the lack of HREE depletion in most of the felsic mantle dikes requires limited garnet in their source rocks, which constrains the depth of melting. To further quantify the amount of garnet permitted in the source of the felsic mantle dikes, we developed both traditional and Monte Carlo modal batch melting models [*Rollinson*, 2014b]. We focused on the dikes with U- to V-shaped REE patterns, which we attribute to partial melting of an amphibolite source. In the Monte Carlo simulation, we varied the weight percent amphibole (15–60 %), clinopyroxene (0–25 %), garnet (0–10 %), titanite (0–5%), and plagioclase (0–85 %; set by difference) in an amphibolite source, and calculated the trace-element composition of equilibrium partial melts. In this modeling, we did not seek to determine the exact mineralogy of the amphibolite source, but instead to explore a range of realistic mineralogies. For comparison, pseudosection modeling of source mineralogies using the Gibbs free energy minimization software Perple_X [*Connolly*, 2005] (see below) suggests modal mineralogies of 30–50 wt. % amphibole, 20–50 wt. % plagioclase, and 10–20% clinopyroxene for amphibolites at solidus temperatures and appropriate pressures for 0–10 wt. % garnet. We used source REE patterns based on the composition of amphibolite samples from the metamorphic sole [*Ishikawa et al*., 2005] or V1 volcanic rocks [*Godard et al*., 2006], which are considered the most likely analogues for the composition of the subducted slab (Supplemental Text S1).

Figure 8 shows our preferred model using the partition coefficients of Rollinson [2015], based on data from Sisson [amphibole; 1994], Bacon and Druitt [amphibole; 1988], and Rubatto and Hermann [garnet; 2007]; the selected partition coefficients are from felsic systems to be consistent with the felsic composition of amphibolite partial melts [*Beard and Lofgren*, 1991; *Rapp et al*., 1991]. The HREE slope of the modeled melts reflect a balance between amphibole and garnet partitioning, where amphibole in the source leads to more positive HREE slopes (i.e., lower Dy/Yb and U- to V- shaped REE patterns), while higher modal garnet decreases the HREE slope (i.e., higher Dy/Yb). Our Monte Carlo models indicate that source rocks with >5 wt. % garnet lead to flatter HREE slopes (higher Dy/Yb) than observed in the dikes (Figure 8; average V1 starting composition); the dike data are most consistent with models of ≤2 wt. % garnet. These results are insensitive to the percent melting.

In reality, even the dikes with U- to V-shaped REE patterns likely incorporated some sediment melt, as indicated by the variable $\varepsilon_{Nd}(t)$. Sediment melts are expected to have flat to HREE depleted REE patterns [this study; *Guo and Wilson*, 2012; *Rollinson*, 2015], and the addition of a sediment melt would further reduce the predicted percentage of garnet in the amphibolite source. Given that we sought to determine the maximum percent garnet that may have existed within the amphibolite source for the felsic mantle dikes, and including sediment melts is most likely to reduce the predicted percentage of garnet in the source, we did not focus on the proportion or composition of sediment melts in the Monte Carlo models. It is possible that some of the low $\varepsilon_{Nd}(t)$ samples that are LREE enriched with flat HREE (Figure 6f) could reflect melting of a garnet-rich amphibolite source (i.e., the flat HREE are a balance between the elevated HREE from the source amphibolite and HREE depletion due to a strong garnet signature); however, given the low $\varepsilon_{Nd}(t)$ of these samples, we consider it more likely that the REE patterns reflect a large sediment component, as previously suggested [*Haase et al*., 2015; *Rollinson*, 2015; *Spencer et al*., 2017].

The extended trace-element patterns of our melting models are generally consistent with the sample data, with the exceptions of the absence of negative Ti anomalies, smaller positive Pb anomalies, higher Zr and Hf concentrations, and lower Rb and Ba concentrations in the model results (Supplemental Figure S2). The higher Zr, Hf, and Ti in the model data likely reflect residual zircon, ilmenite, and/or titanite in the source [*Rollinson*, 2015], the low Rb and Ba are due to depletions of these elements in the selected source composition and the higher Pb observed in the samples may reflect contributions from a sediment or fluid component. In terms of the HREE slope, any residual zircon in the source would flatten the HREE and further limited the predicted modal percent garnet.

To test the sensitivity of the model results to the assumed source composition and the presence of titanite in the source, we modeled melting of a range of V1 and sole compositions and ran models containing 0–5 wt. % titanite. Given that partition coefficients (Kd) can be sensitive to mineral composition, melt composition, *P,* and *T*, we further tested our models using a range of published coefficients for amphibole, clinopyroxene, garnet, and titanite. The results of these additional models are discussed in the Supplemental Text S1 and plotted in Supplemental Figures S3–8, and further support the conclusion that the amphibolite source for the felsic mantle dikes likely contained <5 wt. % garnet.

The relative percentage of amphibole and plagioclase in the best-fit models is somewhat dependent on the source composition. Either of the average compositions we focused on (average Salahi V1 or clinopyroxene free, high-grade amphibolites) can reproduce four of the five data points from the felsic mantle dikes, but the best fit models, especially for the sole amphibolite starting composition, have less amphibole (10–40 wt. %) and more plagioclase (30–90 wt. %) than the predicted amphibolite mineralogy at the appropriate *P-T* based on pseudosection modeling. However, the apparent "excess" plagioclase in the source may actually reflect fractional crystallization of plagioclase from the melts (i.e., we are modeling the dike REE based on melting alone, but their chemistry likely reflects a combination of source melting and subsequent fractional crystallization). As such, we do not expect the relative proportions of amphibole and plagioclase to necessarily match the mineralogy of the source amphibolite. The amount of plagioclase in the source (or removed during fractional crystallization) primarily changes the LREE slope (i.e. Ce/Sm) and does not significantly impact the HREE slope, and therefore does not impact the predicted percent garnet in the source.

Overall, our modeling suggests that the REE patterns of the felsic mantle dikes are most consistent with <5 wt. % garnet in the amphibolite source. To understand pressure and temperature bounds for felsic dike generation that are consistent with this result, we performed thermodynamic modelling using the Gibbs free-energy minimization software Perple_X v. 6.8.4 [*Connolly*, 2005] (Supplemental Text S1). These efforts were applied to seven subdivisions of the potential source compositions outlined above, with the primary bulk compositions used in the trace-element modelling highlighted (blue and red lines).

Based on the melt partitioning results, the source conditions for the high-ε_{Nd} dikes with U- to V- shaped HREE patterns are bounded by the wet solidus (at low T) and the occurrence of the 5 wt. % garnet modal isopleth (at high *P*); these are combined and displayed for each of the modeled bulk compositions in Figure 9. Most of the possible source rocks exhibit solidus temperatures between 700–800°C, and maximum pressures for 5 wt. % garnet between 1.0–1.4 GPa, but there are clear differences between different bulk compositions. For example, models using the bulk composition of the highest-grade, garnet-bearing sole amphibolites have a distinctly higher-*T* solidus (potentially reflecting prior melt extraction and significant Ca enrichments relative to other starting compositions), whereas models using the composition of the lowest-grade, garnet-free sole amphibolites exhibit far more garnet over the investigated *P-T* range than any other composition (reflecting higher bulk-rock FeO and MnO contents). Overall, the pseudosection results are consistent with high-ε_{Nd} dike generation by wet melting at $P \leq 1.4$ GPa and $T \geq 700$–750 °C, which broadly matches the *P-T* conditions recorded by sole amphibolites [*Cowan et al*., 2014; *Searle and Cox*, 2002b; *Soret et al*., 2017].

7. Conclusions

The origin of felsic intrusions into the upper mantle and lower crust of the Samail ophiolite have been the focus of several recent studies. Here we build on these contributions by presenting an integrated dataset of whole rock major-element, trace-element and Nd-isotopic data from intrusions from a wider geographic area. The new and published data suggest three distinct mixing and fractionation trends. Most of the intrusions in Oman formed primarily by mixing between amphibolite and metasediment melts, with little mantle contribution. In contrast, the well-studied dike swarm at Wadi Hajr and Wadi Hemli in the southern Haylayn massif formed through three-component mixing between amphibolite-metasediment melts and a mantle component, consistent with prior research [*Haase et al*., 2015; *Rollinson*, 2014a; 2015]. Finally, a single sample with high ε_{Nd} and an LREE-depleted trace element signature likely formed by differentiation of depleted, mantle derived magmas related to the V2 magmatic series. U-Pb zircon dates from the Oman dikes show that the V2-related dike intruded earlier, at 95.478 ± 0.032 Ma, while the rest of the dated dikes have near synchronous, younger dates of 95.201 ± 0.032 Ma to 94.95 ± 0.10 along the length of the ophiolite in Oman [*Rioux et al*., in review]. Combined geochemical and pseudosection modeling suggests that the dikes were generated by partial melting of underthrust material at $P \leq 1.4$ GPa and $T \geq 700$–750 °C. The distinct mixing trends of the dikes may reflect heterogeneities in thermal conditions within the mantle wedge and/or at the top of the underthrust or subducted slab and heterogeneities in the proportion of amphibolites and metasediments along any given portion of the underthrust plate. Felsic intrusions into the mantle in the UAE follow similar mixing trends to the Oman samples, with most reflecting primarily two-component mixing between amphibolite and metasediment melts, consistent with the conclusions of Cox et al. [1999]; however, U-Pb dates from the felsic dikes intruding the northern termination of the ophiolite in the UAE range from 94.119 ± 0.057 to 90.998 ± 0.052 Ma [*Rioux et al*., in review], indicating that felsic magmatism there significantly post-dated all other magmatic events (both mafic and felsic) recorded in the bulk of the ophiolite.

Acknowledgements:

This research was supported by United States National Science Foundation grants EAR-1250522 and 1650407 to Matthew Rioux. We thank the Public Authority for Mining for their support of our research in the Sultanate of Oman, and Mohammed Ali and Aisha Al Suwaidi at Khalifa University for their contributions to our work in the United Arab Emirates. We are grateful for insightful reviews by Karsten Haase, an anonymous reviewer, and Editor Steve Parman, which substantially improved this manuscript. Joshua Garber acknowledges support from National Science Foundation grant OISE-1545903 and The Pennsylvania State University. Geochemical data from this study are available on the EarthChem Library using the following links:

- Table 2 major- and trace-element data: https://doi.org/10.26022/IEDA/111896
- Table 2 isotopic data: https://doi.org/10.26022/IEDA/111897
- Table 3 major- and trace-element data: https://doi.org/10.26022/IEDA/111894
- Table 3 isotopic data: https://doi.org/10.26022/IEDA/111895

Figure Captions

Figure. 1. Geologic map of the Samail ophiolite [after *Nicolas et al*., 2000] showing the location of felsic mantle dikes from this and previous geochemical studies. Larger symbols and text denote samples from this study. Smaller green squares are samples from Rioux et al. (2013, in review) with no whole rock isotope and/or geochemical data. Densely sampled locations from the southern Haylayn massif are offset slightly for clarity. Briqueu et al. [1991] focused on similar areas to the Cox et al. [1999] localities. Massif names are in italics. Map after Nicolas et al. [2000]. Plot symbol shapes are consistent with Figures 2, 3, and 5.

Figure. 2. Composition of felsic mantle dikes from Oman (a, c, e) and the United Arab Emirates (b, d, f). Larger plot symbols denote data from this study. Plutonic rocks associated with the V1 and V2 magmatic series are included for comparison [*Haase et al*., 2016; *Rollinson*, 2009]. The Haylayn group only includes samples from Wadi Hajr and Wadi Hemli, in the southern Haylayn massif; two samples from the northern Haylayn massif are grouped with the "Other Oman" samples. (a-b) CIPW normative compositions of the felsic mantle dikes. Himalayan leucogranite field is after Rollinson [2015], based on data from Guo and Wilson [2012]; plutonic fields are after Barker [1979]. (c-d) Aluminum saturation index (molar Al_2O_3/[(CaO-3.34*P_2O_5)+Na_2O+K_2O) [*Frost et al*., 2001] versus molar $Al_2O_3/(Na_2O + K_2O)$. (e-f) Weight percent K_2O versus normalized Ce/Dy. Data sources are listed in the Figure 3 caption.

Figure 3. Major-element variation diagrams. V1 and V2 data with MgO = 10–14 wt. % plot off scale. Data sources: felsic mantle dikes [this study; *Amri et al*., 2007; *Cox et al*., 1999; *Haase et al*., 2015; *Rollinson*, 2014a; 2015], V1 and V2 volcanic rocks [*Godard et al*., 2003; *Godard et al*., 2006; *Kusano et al*., 2012; *Kusano et al*., 2014; *Kusano et al*., 2017], V1 and V2 plutonic rocks [*Amri et al*., 2007; *Haase et al*., 2016; *Rioux et al*., 2016; *Tsuchiya et al*., 2013]. The V1 and V2 plutonic rocks are plotted based on how the data were grouped in the source publications; however, we note that robust distinction between the V1 and V2 related plutonic rocks requires a combination of field observations and geochemical data, which are not reported in all studies. The upper V2 volcanic series corresponds to the upper V2 lavas of Kusano et al. [2017], with the addition of a single lower V2 lava with low ε_{Nd} (sample 10SH21). 'Amph. melt' data are liquid compositions from amphibolite melting experiments by Rapp et al. [1991], Rushmer [1991], and Zhang et al. [2013].

Figure 4. Rare earth element (REE) and extended trace element diagrams for magmatic series in the Samail ophiolite. Panel (a) includes data for the sole metasediment reported herein. Data sources: felsic mantle dikes from the southern Haylayn massif (Wadi Hajr and Wadi Hemli) [*Haase et al*., 2015; *Rollinson*, 2014a; 2015]; felsic mantle dikes from other areas of Oman [*Amri et al*., 2007; *Rollinson*, 2015]; felsic mantle dikes in the UAE [*Rollinson*, 2015]; V1 and V2 volcanic rocks [*Godard et al*., 2003; *Godard et al*., 2006]. For a discussion of the origin of the flat REE patterns with large negative Eu anomalies from the Ra's Dadnah area in the UAE, see Rollinson [2015]. REE diagrams are normalized to Anders and Grevesse [1989] multiplied by 1.36 [*Korotev*, 1996] and extended trace element diagrams are normalized to normal mid-ocean ridge

basalt [*Hofmann*, 1988]. Sample 13217M01 is highlighted in panel (a), but is also plotted in panel (c).

Figure 5. Major-element, trace-element and isotope variation diagrams. Felsic mantle dikes are divided into intrusions in the southern Haylayn massif (diamonds), intrusions from the rest of the ophiolite sections in Oman (squares), and intrusions in the UAE portion of the ophiolite (open circles). Symbol colors for the Oman dikes are based on data groupings shown in (a) and described in the text. Smaller gray and black symbols for the dikes in (d, e, f, g) correspond to geochemical data that lack Nd isotopic data. The V1 and V2 datasets include analyses from volcanic and plutonic rocks attributed to these magmatic events. Data sources are provided in Supplemental Figure S1. Additional sources include the following: (b) amphibolite melting experiments [*Rapp et al.*, 1991; *Rushmer*, 1991; *Zhang et al.*, 2013]; (e) discrimination diagram [*Patiño Douce*, 1999; *Rollinson*, 2015]; (h) sediment and amphibolite Zr/Sm [*Foley et al.*, 2002; *Guo and Wilson*, 2012]. Abbreviations: sed., sediment; amph., amphibolite; inc., increasing; exp. experiments.

Figure 6. Rare-earth element (REE) plots for felsic dikes that intrude the mantle and lowermost crust in Oman. The data are divided based on whole rock ε_{Nd}, with plot colors corresponding to the color scheme in Figure 5. REE patterns from the Lasail and Alley components of the V2 series are included in (a) for comparison. The 20% amphibolite melt was modeled using the parameters described in Figure 8, with 0% garnet. Data sources: felsic mantle dike REE [this study; *Amri et al.*, 2007; *Haase et al.*, 2015]; amphibolite+sediment melt model [*Rollinson*, 2015]; Sediment 13222M06 composition [*Garber et al.*, 2020]; Lasail and Alley REE patterns [*Godard et al.*, 2003; *Godard et al.*, 2006]. Data are normalized to Anders and Grevesse [1989] multiplied by 1.36 [*Korotev*, 1996]. This figure only includes samples with both REE and Nd isotopic data.

Figure 7. Extended trace element diagrams for felsic dikes that intrude the mantle and lowermost crust in Oman. Data are grouped following the trends defined in Figure 5. V1 lavas [*Godard et al.*, 2003; *Godard et al.*, 2006] and the composition of a sole metasediment (13222M06) are shown for comparison. Normalized to normal mid-ocean ridge basalt [*Hofmann*, 1988].

Figure 8. (a) Monte Carlo simulations of batch partial melting of an amphibolite source with 0–10 wt. % garnet (n = 2000 iterations per garnet step), compared to data from low MgO, $\varepsilon_{Nd}(t) > -2$, felsic mantle dikes with U- to V- shaped REE (green squares in Figure 5). Proportions of amphibole, plagioclase, and clinopyroxene were varied, as described in the text—this model has 0% titanite. The model is for 20% batch modal melting of an average V1 composition (Geotimes from Wadi Salahi) [*Godard et al.*, 2006], using the distribution coefficients from Rollinson [2015]. Inc. amph./dec. plag., increasing wt. % amphibole and decreasing wt. % plagioclase; inc. garnet, increasing wt. % garnet. (b) Model results showing the impact of 0, 2, 5, and 10 wt. % garnet in the source, compared to the REE patterns of the felsic mantle dikes (gray lines; $\varepsilon_{Nd}(t) > -2$). The plotted REE patterns are for 20% batch modal melting of an amphibolite source with ~25 wt. % amphibole, ~60 w.t % plagioclase, and 15 wt. % clinopyroxene. Data are normalized to Anders and Grevesse [1989] multiplied by 1.36 [*Korotev*, 1996].

Figure 9. (a) Calculated bounds on high-$\varepsilon_{Nd}(t)$ dike generation from Perple_X [*Connolly*, 2005]. Each line represents constraints from a single bulk composition, with the low-*T* (near vertical) bound representing the H_2O-saturated solidus and the high-*P* (near horizontal) bound representing

the 5 wt.% garnet modal isopleth (i.e., viable source conditions are on the high-T, low-P side of each line). The average V1 Salahi and sole amphibolite compositions used in our geochemical modeling are highlighted. All lines were smoothed for clarity. (b) P-T conditions of the wet solidus and garnet isopleths for the average V1 Salahi composition.

References Cited

Adachi, Y., and S. Miyashita (2003), Geology and petrology of the plutonic complexes in the Wadi Fizh area: Multiple magmatic events and segment structure in the northern Oman ophiolite, *Geochemistry, Geophysics, Geosystems*, *4*(9), 8619.
Adam, J., and T. H. Green (1994), The effects of pressure and temperature on the partitioning of Ti, Sr and REE between amphibole, clinopyroxene and basanitic melts, *Chemical Geology*, *117*(1), 219-233.
Adam, J., T. H. Green, and S. H. Sie (1993), Proton microprobe determined partitioning of Rb, Sr, Ba, Y, Zr, Nb and Ta between experimentally produced amphiboles and silicate melts with variable F content, *Chemical Geology*, *109*(1), 29-49.
Alabaster, T., J. A. Pearce, and J. Malpas (1982), The volcanic stratigraphy and petrogenesis of the Oman ophiolite complex, *Contributions to Mineralogy and Petrology*, *81*(3), 168-183.
Aldiss, D. T. (1981), Plagiogranites from the ocean crust and ophiolites, *Nature*, *289*(5798), 577-578.
Amri, I., M. Benoit, and G. Ceuleneer (1996), Tectonic setting for the genesis of oceanic plagiogranites: Evidence from a paleo-spreading structure in the Oman ophiolite, *Earth and Planetary Science Letters*, *139*(1-2), 177-194.
Amri, I., G. Ceuleneer, M. Benoit, M. Python, E. Puga, and K. Targuisti (2007), Genesis of granitoids by interaction between mantle peridotites and hydrothermal fluids in oceanic spreading setting in the Oman ophiolite, *Geogaceta*, *42*, 23-26.
Anders, E., and N. Grevesse (1989), Abundances of the elements: Meteoritic and solar, *Geochimica et Cosmochimica Acta*, *53*(1), 197-214.
Aries, S., M. Valladon, M. Polvé, and B. Dupré (2000), A Routine Method for Oxide and Hydroxide Interference Corrections in ICP-MS Chemical Analysis of Environmental and Geological Samples, *Geostandards Newsletter*, *24*(1), 19-31.
Bachmann, O., M. A. Dungan, and F. Bussy (2005), Insights into shallow magmatic processes in large silicic magma bodies: the trace element record in the Fish Canyon magma body, Colorado, *Contributions to Mineralogy and Petrology*, *149*(3), 338-349.
Bacon, C. R., and T. H. Druitt (1988), Compositional evolution of the zoned calcalkaline magma chamber of Mount Mazama, Crater Lake, Oregon, *Contributions to Mineralogy and Petrology*, *98*(2), 224-256.
Bailey, E. H. (1981), Geologic map of Muscat-Ibra area, Sultanate of Oman *J. Geophys. Res.*, *86*(B4), map.
Barker, F. (1979), Chapter 1 - Trondhjemite: Definition, Environment and Hypotheses of Origin, in *Developments in Petrology*, edited by F. Barker, pp. 1-12, Elsevier.
Beard, J. S., and G. E. Lofgren (1991), Dehydration Melting and Water-Saturated Melting of Basaltic and Andesitic Greenstones and Amphibolites at 1, 3, and 6. 9 kb, *Journal of Petrology*, *32*(2), 365-401.
Bédard, J. H. (2014), Parameterizations of calcic clinopyroxene—Melt trace element partition coefficients, *Geochemistry, Geophysics, Geosystems*, *15*(2), 303-336.

Benoit, M., M. Polvé, and G. Ceuleneer (1996), Trace element and isotopic characterization of mafic cumulates in a fossil mantle diapir (Oman ophiolite), *Chemical Geology*, *134*(1-3), 199-214.
Benoit, M., G. Ceuleneer, and M. Polve (1999), The remelting of hydrothermally altered peridotite at mid-ocean ridges by intruding mantle diapirs, *Nature*, *402*(6761), 514-518.
Boudier, F., G. Ceuleneer, and A. Nicolas (1988), Shear zones, thrusts and related magmatism in the Oman ophiolite: Initiation of thrusting on an oceanic ridge, *Tectonophysics*, *151*(1-4), 275-296.
Braun, J.-J., J. Viers, B. Dupré, M. Polve, J. Ndam, and J.-P. Muller (1998), Solid/Liquid REE Fractionation in the Lateritic System of Goyoum, East Cameroon: The Implication for the Present Dynamics of the Soil Covers of the Humid Tropical Regions, *Geochimica et Cosmochimica Acta*, *62*(2), 273-299.
Brenan, J. M., H. F. Shaw, F. J. Ryerson, and D. L. Phinney (1995), Experimental determination of trace-element partitioning between pargasite and a synthetic hydrous andesitic melt, *Earth and Planetary Science Letters*, *135*(1), 1-11.
Briqueu, L., C. Mével, and F. Boudier (1991), Sr, Nd and Pb isotopic constraints on the genesis of a calc-alkaline plutonic suite in the Oman mountains related to the obduction process, in *Ophiolite genesis and evolution of the oceanic lithosphere*, edited by P. Tea, pp. 517–542, Ministry of Petroleum and Minerals, Sultanate of Oman.
Browning, P., and J. D. Smewing (1981), Processes in magma chambers beneath spreading axes: evidence from magmatic associations in the Oman Ophiolite, *Journal of the Geological Society, London*, *138*(3), 279-280.
Ceuleneer, G., M. Monnereau, and I. Amri (1996), Thermal structure of a fossil mantle diapir inferred from the distribution of mafic cumulates, *Nature*, *379*(6561), 149-153.
Coleman, R. G., and C. A. Hopson (1981), Introduction to the Oman Ophiolite Special Issue, *Journal of Geophysical Research: Solid Earth*, *86*(B4), 2495-2496.
Connolly, J. A. D. (2005), Computation of phase equilibria by linear programming: A tool for geodynamic modeling and its application to subduction zone decarbonation, *Earth and Planetary Science Letters*, *236*(1–2), 524-541.
Cowan, R. J., M. P. Searle, and D. J. Waters (2014), Structure of the metamorphic sole to the Oman Ophiolite, Sumeini Window and Wadi Tayyin: implications for ophiolite obduction processes, *Geological Society, London, Special Publications*, *392*(1), 155-175.
Cox, J., M. Searle, and R. Pedersen (1999), The petrogenesis of leucogranitic dykes intruding the northern Semail ophiolite, United Arab Emirates: field relationships, geochemistry and Sr/Nd isotope systematics, *Contributions to Mineralogy and Petrology*, *137*(3), 267-287.
Dalpé, C., and D. R. Baker (2000), Experimental investigation of large-ion-lithophile-element-, high-field-strength-element- and rare-earth-element-partitioning between calcic amphibole and basaltic melt: the effects of pressure and oxygen fugacity, *Contributions to Mineralogy and Petrology*, *140*(2), 233-250.
Ernewein, M., C. Pflumio, and H. Whitechurch (1988), The death of an accretion zone as evidenced by the magmatic history of the Sumail ophiolite (Oman), *Tectonophysics*, *151*(1-4), 247-274.
Foley, S., M. Tiepolo, and R. Vannucci (2002), Growth of early continental crust controlled by melting of amphibolite in subduction zones, *Nature*, *417*(6891), 837-840.

France, L., B. Ildefonse, and J. Koepke (2009), Interactions between magma and hydrothermal system in Oman ophiolite and in IODP Hole 1256D: Fossilization of a dynamic melt lens at fast spreading ridges, *Geochem. Geophys. Geosyst.*, *10*(10), Q10O19.
Frost, B. R., C. G. Barnes, W. J. Collins, R. J. Arculus, D. J. Ellis, and C. D. Frost (2001), A Geochemical Classification for Granitic Rocks, *Journal of Petrology*, *42*(11), 2033-2048.
Fuhrman, M. L., and D. H. Lindsley (1988), Ternary-feldspar modeling and thermometry, *American Mineralogist*, *73*(3-4), 201-215.
Garber, J. M., M. Rioux, A. R. C. Kylander-Clark, B. R. Hacker, J. D. Vervoort, and M. P. Searle (2020), Petrochronology of Wadi Tayin Metamorphic Sole Metasediment, With Implications for the Thermal and Tectonic Evolution of the Samail Ophiolite (Oman/UAE), *Tectonics*, *39*(12), e2020TC006135.
Ghent, E. D., and M. Z. Stout (1981), Metamorphism at the Base of the Samail Ophiolite, Southeastern Oman Mountains, *J. Geophys. Res.*, *86*(B4), 2557-2571.
Gnos, E. (1998), Peak Metamorphic Conditions of Garnet Amphibolites Beneath the Semail Ophiolite: Implications for an Inverted Pressure Gradient, *International Geology Review*, *40*(4), 281-304.
Godard, M., J. M. Dautria, and M. Perrin (2003), Geochemical variability of the Oman ophiolite lavas: Relationship with spatial distribution and paleomagnetic directions, *Geochem. Geophys. Geosyst.*, *4*(6), 8609.
Godard, M., D. Bosch, and F. Einaudi (2006), A MORB source for low-Ti magmatism in the Semail ophiolite, *Chemical Geology*, *234*(1-2), 58-78.
Green, E. C. R., R. W. White, J. F. A. Diener, R. Powell, T. J. B. Holland, and R. M. Palin (2016), Activity–composition relations for the calculation of partial melting equilibria in metabasic rocks, *Journal of Metamorphic Geology*, *34*(9), 845-869.
Guo, Z., and M. Wilson (2012), The Himalayan leucogranites: Constraints on the nature of their crustal source region and geodynamic setting, *Gondwana Research*, *22*(2), 360-376.
Haase, K. M., S. Freund, J. Koepke, F. Hauff, and M. Erdmann (2015), Melts of sediments in the mantle wedge of the Oman ophiolite, *Geology*.
Haase, K. M., S. Freund, C. Beier, J. Koepke, M. Erdmann, and F. Hauff (2016), Constraints on the magmatic evolution of the oceanic crust from plagiogranite intrusions in the Oman ophiolite, *Contributions to Mineralogy and Petrology*, *171*(5), 1-16.
Hacker, B. R., and J. L. Mosenfelder (1996), Metamorphism and deformation along the emplacement thrust of the Samail ophiolite, Oman, *Earth and Planetary Science Letters*, *144*(3-4), 435-451.
Hilyard, M., R. L. Nielsen, J. S. Beard, A. Patinõ-Douce, and J. Blencoe (2000), Experimental determination of the partitioning behavior of rare earth and high field strength elements between pargasitic amphibole and natural silicate melts, *Geochimica et Cosmochimica Acta*, *64*(6), 1103-1120.
Hofmann, A. W. (1988), Chemical differentiation of the Earth: the relationship between mantle, continental crust, and oceanic crust, *Earth and Planetary Science Letters*, *90*(3), 297-314.
Holland, T. J. B., and R. Powell (1991), A Compensated-Redlich-Kwong (CORK) equation for volumes and fugacities of CO2 and H2O in the range 1 bar to 50 kbar and 100–1600°C, *Contributions to Mineralogy and Petrology*, *109*(2), 265-273.
Holland, T. J. B., and R. Powell (2011), An improved and extended internally consistent thermodynamic dataset for phases of petrological interest, involving a new equation of state for solids, *Journal of Metamorphic Geology*, *29*(3), 333-383.

Ishikawa, T., K. Nagaishi, and S. Umino (2002), Boninitic volcanism in the Oman ophiolite: Implications for thermal condition during transition from spreading ridge to arc, *Geology*, *30*(10), 899-902.
Ishikawa, T., S. Fujisawa, K. Nagaishi, and T. Masuda (2005), Trace element characteristics of the fluid liberated from amphibolite-facies slab: Inference from the metamorphic sole beneath the Oman ophiolite and implication for boninite genesis, *Earth and Planetary Science Letters*, *240*(2), 355-377.
Johnson, D., P. Hooper, and R. Conrey (1999), XRF Method XRF Analysis of Rocks and Minerals for Major and Trace Elements on a Single Low Dilution Li-Tetraborate Fused Bead, *Adv. X-ray anal*, *41*, 843-867.
Kelly, D. (2018), Analysis of geological materials by low dilution fusion at the Peter Hooper GeoAnalytical Lab (Washington State University), Washington State University, Pullman, WA, USA.
Klein, M., H. G. Stosch, and H. A. Seck (1997), Partitioning of high field-strength and rare-earth elements between amphibole and quartz-dioritic to tonalitic melts: an experimental study, *Chemical Geology*, *138*(3), 257-271.
Klein, M., H. G. Stosch, H. A. Seck, and N. Shimizu (2000), Experimental partitioning of high field strength and rare earth elements between clinopyroxene and garnet in andesitic to tonalitic systems, *Geochimica et Cosmochimica Acta*, *64*(1), 99-115.
Knaack, C., S. Cornelius, and P. Hooper (1994), Trace element analyses of rocks and minerals by ICP-MS, *Washington State University, Open-File Report*.
Koepke, J., S. T. Feig, J. Snow, and M. Freise (2004), Petrogenesis of oceanic plagiogranites by partial melting of gabbros: An experimental study, *Contributions to Mineralogy and Petrology*, *146*(4), 414-432.
Korotev, R. L. (1996), A self-consistent compilation of elemental concentration data for 93 geochemical reference samples, *Geostandards Newsletter*, *20*(2), 217-245.
Kusano, Y., Y. Adachi, S. Miyashita, and S. Umino (2012), Lava accretion system around mid-ocean ridges: Volcanic stratigraphy in the Wadi Fizh area, northern Oman ophiolite, *Geochem. Geophys. Geosyst.*, *13*, Q05012.
Kusano, Y., M. Hayashi, Y. Adachi, S. Umino, and S. Miyashita (2014), Evolution of volcanism and magmatism during initial arc stage: constraints on the tectonic setting of the Oman Ophiolite, *Geological Society, London, Special Publications*, *392*(1), 177.
Kusano, Y., S. Umino, R. Shinjo, A. Ikei, Y. Adachi, S. Miyashita, and S. Arai (2017), Contribution of slab-derived fluid and sedimentary melt in the incipient arc magmas with development of the paleo-arc in the Oman Ophiolite, *Chemical Geology*, *449*, 206-225.
LaTourrette, T., R. L. Hervig, and J. R. Holloway (1995), Trace element partitioning between amphibole, phlogopite, and basanite melt, *Earth and Planetary Science Letters*, *135*(1), 13-30.
Lippard, S. J., A. W. Shelton, and I. G. Gass (1986), *The Ophiolite of Northern Oman*, 178 pp., Geological Society, London, London.
MacLeod, C. J., and G. Yaouancq (2000), A fossil melt lens in the Oman ophiolite: Implications for magma chamber processes at fast spreading ridges, *Earth and Planetary Science Letters*, *176*(3-4), 357-373.
MacLeod, C. J., C. J. Lissenberg, and L. E. Bibby (2013), "Moist MORB" axial magmatism in the Oman ophiolite: The evidence against a mid-ocean ridge origin, *Geology*.
Mahood, G., and W. Hildreth (1983), Large partition coefficients for trace elements in high-silica rhyolites, *Geochimica et Cosmochimica Acta*, *47*(1), 11-30.

Maunder, B., J. Prytulak, S. Goes, and M. Reagan (2020), Rapid subduction initiation and magmatism in the Western Pacific driven by internal vertical forces, *Nature Communications*, *11*(1), 1874.
McCulloch, M. T., R. T. Gregory, G. J. Wasserburg, and H. P. Taylor (1981), Sm-Nd, Rb-Sr, and $^{18}O/^{16}O$ isotopic systematics in an oceanic crustal section: Evidence from the Samail Ophiolite, *J. Geophys. Res.*, *86*(B4), 2721-2735.
Natland, J. H., and H. J. B. Dick (2002), Stratigraphy and composition of gabbros drilled in Ocean Drilling Program Hole 735B, Southwest Indian Ridge; a synthesis of geochemical data, *Proceedings of the Ocean Drilling Program, Scientific Results*, *176*.
Nicolas, A., F. Boudier, B. Ildefonse, and E. Ball (2000), Accretion of Oman and United Arab Emirates ophiolite – Discussion of a new structural map, *Marine Geophysical Research*, *21*(3), 147-180.
Nicolas, A., F. Boudier, J. Koepke, L. France, B. Ildefonse, and C. Mevel (2008), Root zone of the sheeted dike complex in the Oman ophiolite, *Geochem. Geophys. Geosyst.*, *9*(5), Q05001.
Nikolaeva, K., T. V. Gerya, and J. A. D. Connolly (2008), Numerical modelling of crustal growth in intraoceanic volcanic arcs, *Physics of the Earth and Planetary Interiors*, *171*(1), 336-356.
Norman, M., M. O. Garcia, and A. J. Pietruszka (2005), Trace-element distribution coefficients for pyroxenes, plagioclase, and olivine in evolved tholeiites from the 1955 eruption of Kilauea Volcano, Hawai'i, and petrogenesis of differentiated rift-zone lavas, *American Mineralogist*, *90*(5-6), 888-899.
Olin, P. H., and J. A. Wolff (2010), Rare earth and high field strength element partitioning between iron-rich clinopyroxenes and felsic liquids, *Contributions to Mineralogy and Petrology*, *160*(5), 761-775.
Olin, P. H., and J. A. Wolff (2012), Partitioning of rare earth and high field strength elements between titanite and phonolitic liquid, *Lithos*, *128–131*, 46-54.
Pallister, J. S., and C. A. Hopson (1981), Samail ophiolite plutonic suite: Field relations, phase variation, cryptic variation and layering, and a model of a spreading ridge magma chamber, *Journal of Geophysical Research*, *86*(B4), 2593-2644.
Patiño Douce, A. E. (1999), What do experiments tell us about the relative contributions of crust and mantle to the origin of granitic magmas?, *Geological Society, London, Special Publications*, *168*(1), 55-75.
Pearce, J. A. (1989), High T/P metamorphism and granite genesis beneath ophiolite thrust sheets, *Ofioliti*, *14*(3), 195-211.
Pearce, J. A., T. Alabaster, A. W. Shelton, and M. P. Searle (1981), The Oman ophiolite as a Cretaceous arc-basin complex: Evidence and implications, *Philosophical Transactions of the Royal Society of London. Series A, Mathematical and Physical Sciences*, *300*(1454), 299-317.
Peters, T., and B. S. Kamber (1994), Peraluminous potassium-rich granitoids in the Semail Ophiolite, *Contributions to Mineralogy and Petrology*, *118*(3), 229-238.
Plank, T., and C. H. Langmuir (1998), The chemical composition of subducting sediment and its consequences for the crust and mantle, *Chemical Geology*, *145*(3–4), 325-394.
Prowatke, S., and S. Klemme (2005), Effect of melt composition on the partitioning of trace elements between titanite and silicate melt, *Geochimica et Cosmochimica Acta*, *69*(3), 695-709.
Python, M., and G. Ceuleneer (2003), Nature and distribution of dykes and related melt migration structures in the mantle section of the Oman ophiolite, *Geochem. Geophys. Geosyst.*, *4*(7), 8612.

Qian, Q., and J. Hermann (2013), Partial melting of lower crust at 10–15 kbar: constraints on adakite and TTG formation, *Contributions to Mineralogy and Petrology*, *165*(6), 1195-1224.
Rapp, R. P., E. B. Watson, and C. F. Miller (1991), Precambrian Granitoids Petrogenesis, Geochemistry and Metallogeny Partial melting of amphibolite/eclogite and the origin of Archean trondhjemites and tonalites, *Precambrian Research*, *51*(1), 1-25.
Rioux, M., S. A. Bowring, P. B. Kelemen, S. Gordon, F. Dudás, and R. Miller (2012), Rapid crustal accretion and magma assimilation in the Oman-U.A.E. ophiolite: High precision U-Pb zircon geochronology of the gabbroic crust, *Journal of Geophysical Research*, *117*.
Rioux, M., S. Bowring, P. Kelemen, S. Gordon, R. Miller, and F. Dudás (2013), Tectonic development of the Samail ophiolite: High-precision U-Pb zircon geochronology and Sm-Nd isotopic constraints on crustal growth and emplacement, *Journal of Geophysical Research*, *118*(5), 2085-2101.
Rioux, M., J. Garber, A. Bauer, S. Bowring, M. Searle, P. Kelemen, and B. Hacker (2016), Synchronous formation of the metamorphic sole and igneous crust of the Semail ophiolite: New constraints on the tectonic evolution during ophiolite formation from high-precision U-Pb zircon geochronology, *Earth and Planetary Science Letters*, *451*, p. 708–195.
Rioux, M., J. Garber, M. Searle, P. Kelemen, S. Miyashita, Y. Adachi, and S. Bowring (in review), High-precision U-Pb zircon dating of late magmatic series in the Semail ophiolite: A record of subduction initiation, *Journal of Geophysical Research*.
Rollinson, H. (2009), New models for the genesis of plagiogranites in the Oman ophiolite, *Lithos*, *112*(3-4), 603-614.
Rollinson, H. (2014a), Plagiogranites from the mantle section of the Oman Ophiolite: models for early crustal evolution, *Geological Society, London, Special Publications*, *392*(1), 247-261.
Rollinson, H. (2015), Slab and sediment melting during subduction initiation: granitoid dykes from the mantle section of the Oman ophiolite, *Contributions to Mineralogy and Petrology*, *170*(3), 1-20.
Rollinson, H. R. (2014b), *Using geochemical data: evaluation, presentation, interpretation*, Routledge.
Rubatto, D., and J. Hermann (2007), Experimental zircon/melt and zircon/garnet trace element partitioning and implications for the geochronology of crustal rocks, *Chemical Geology*, *241*(1), 38-61.
Rushmer, T. (1991), Partial melting of two amphibolites: contrasting experimental results under fluid-absent conditions, *Contributions to Mineralogy and Petrology*, *107*(1), 41-59.
Searle, M., and J. Cox (2002a), Subduction zone metamorphism during formation and emplacement of the Semail ophiolite in the Oman Mountains, *Geological Magazine*, *139*(3), 241-255.
Searle, M. P. (1985), Sequence of thrusting and origin of culminations in the northern and central Oman Mountains, *Journal of Structural Geology*, *7*(2), 129-143.
Searle, M. P., and J. Malpas (1980), The structure and metamorphism of rocks beneath the Semail Ophiolite of Oman and their significance in ophiolite obduction, *Transactions of the Royal Society of Edinburgh, Earth Sciences*, *71*, 247–262.
Searle, M. P., and J. Malpas (1982), Petrochemistry and origin of sub-ophiolitic metamorphic and related rocks in the Oman Mountains, *Journal of the Geological Society, London*, *139*(3), 235-248.

Searle, M. P., and J. Cox (2002b), Subduction zone metamorphism during formation and emplacement of the Semail ophiolite in the Oman Mountains, *Geological Magazine*, *139*(3), 241-255.
Searle, M. P., S. J. Lippard, J. D. Smewing, and D. C. Rex (1980), Volcanic rocks beneath the Semail Ophiolite nappe in the northern Oman mountains and their significance in the Mesozoic evolution of Tethys, *Journal of the Geological Society, London*, *137*(5), 589-604.
Searle, M. P., D. J. Waters, J. M. Garber, M. Rioux, A. G. Cherry, and T. K. Ambrose (2015), Structure and metamorphism beneath the obducting Oman ophiolite: Evidence from the Bani Hamid granulites, northern Oman mountains, *Geosphere*.
Sisson, T. W. (1991), Pyroxene-high silica rhyolite trace element partition coefficients measured by ion microprobe, *Geochimica et Cosmochimica Acta*, *55*(6), 1575-1585.
Sisson, T. W. (1994), Hornblende-melt trace-element partitioning measured by ion microprobe, *Chemical Geology*, *117*(1), 331-344.
Sisson, T. W., and C. R. Bacon (1992), Garnet/high-silica rhyolite trace element partition coefficients measured by ion microprobe, *Geochimica et Cosmochimica Acta*, *56*(5), 2133-2136.
Soret, M., P. Agard, B. Dubacq, A. Plunder, and P. Yamato (2017), Petrological evidence for stepwise accretion of metamorphic soles during subduction infancy (Semail ophiolite, Oman and UAE), *Journal of Metamorphic Geology*, *35*(9), 1051-1080.
Spencer, C. J., A. J. Cavosie, T. D. Raub, H. Rollinson, H. Jeon, M. P. Searle, J. A. Miller, B. J. McDonald, N. J. Evans, and F. the Edinburgh Ion Microprobe (2017), Evidence for melting mud in Earth's mantle from extreme oxygen isotope signatures in zircon, *Geology*, *45*(11), 975-978.
Steenberg, L., S. Boroughs, and C. Knaack (2017), Estimation of accuracy and precision for trace elements analyzed by inductively coupled plasma mass spectrometry (ICP-MS) at the Peter Hooper Geoanalytical Laboratory, Washington State University, in *Geological Society of America Annual Meeting*, edited, Geological Society of America Abstracts with Programs, Seattle, Washington.
Taylor, R. J. M., S. L. Harley, R. W. Hinton, S. Elphick, C. Clark, and N. M. Kelly (2015), Experimental determination of REE partition coefficients between zircon, garnet and melt: a key to understanding high-T crustal processes, *Journal of Metamorphic Geology*, *33*(3), 231-248.
Tiepolo, M., R. Oberti, and R. Vannucci (2002), Trace-element incorporation in titanite: constraints from experimentally determined solid/liquid partition coefficients, *Chemical Geology*, *191*(1), 105-119.
Tiepolo, M., R. Oberti, A. Zanetti, R. Vannucci, and S. F. Foley (2007), Trace-element partitioning between amphibole and silicate melt, *Reviews in mineralogy and geochemistry*, *67*(1), 417-452.
Tiepolo, M., R. Vannucci, P. Bottazzi, R. Oberti, A. Zanetti, and S. Foley (2000), Partitioning of rare earth elements, Y, Th, U, and Pb between pargasite, kaersutite, and basanite to trachyte melts: Implications for percolated and veined mantle, *Geochemistry, Geophysics, Geosystems*, *1*(8).
Tsuchiya, N., T. Shibata, M. Yoshikawa, Y. Adachi, S. Miyashita, T. Adachi, N. Nakano, and Y. Osanai (2013), Petrology of Lasail plutonic complex, northern Oman ophiolite, Oman: An example of arc-like magmatism associated with ophiolite detachment, *Lithos*, *156–159*, 120-138.
Usui, Y., and S. Yamazaki (2010), Salvaging primary remanence from hydrothermally altered oceanic gabbros in the Oman ophiolite: A selective destructive demagnetization approach, *Physics of the Earth and Planetary Interiors*, *181*(1–2), 1-11.

White, R., R. Powell, and T. Johnson (2014a), The effect of Mn on mineral stability in metapelites revisited: New a–x relations for manganese-bearing minerals, *Journal of Metamorphic Geology*, *32*(8), 809-828.
White, R. W., R. Powell, and G. L. Clarke (2002), The interpretation of reaction textures in Fe-rich metapelitic granulites of the Musgrave Block, central Australia: constraints from mineral equilibria calculations in the system K2O–FeO–MgO–Al2O3–SiO2–H2O–TiO2–Fe2O3, *Journal of Metamorphic Geology*, *20*(1), 41-55.
White, R. W., R. Powell, T. J. B. Holland, T. E. Johnson, and E. C. R. Green (2014b), New mineral activity–composition relations for thermodynamic calculations in metapelitic systems, *Journal of Metamorphic Geology*, *32*(3), 261-286.
Wilson, D. S., et al. (2006), Drilling to Gabbro in Intact Ocean Crust, *Science*, *312*(5776), 1016.
Zhang, C., F. Holtz, J. Koepke, P. E. Wolff, C. Ma, and J. H. Bédard (2013), Constraints from experimental melting of amphibolite on the depth of formation of garnet-rich restites, and implications for models of Early Archean crustal growth, *Precambrian Research*, *231*, 206-217.

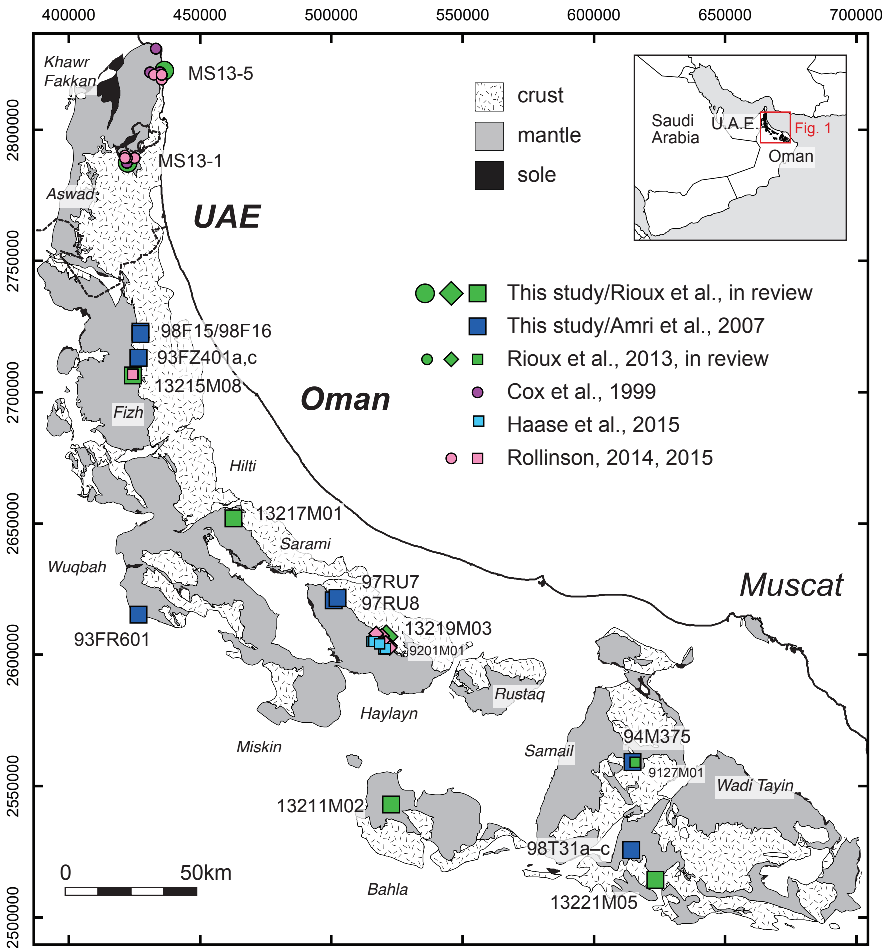

400000
450000
500000
550000
600000
650000
700000
2800000
2750000
2700000
2650000
2600000
2550000
2500000
Khawr Fakkan
MS13-5
MS13-1
Aswad
UAE
crust
mantle
sole
Saudi Arabia
U.A.E.
Fig. 1
Oman
This study/Rioux et al., in review
This study/Amri et al., 2007
Rioux et al., 2013, in review
Cox et al., 1999
Haase et al., 2015
Rollinson, 2014, 2015
98F15/98F16
93FZ401a,c
13215M08
Fizh
Oman
Hilti
13217M01
Sarami
Wuqbah
97RU7
97RU8
93FR601
13219M03
9201M01
Muscat
Rustaq
Haylayn
Miskin
Samail
94M375
9127M01
Wadi Tayin
13211M02
98T31a–c
13221M05
Bahla
0
50km

Figure 1

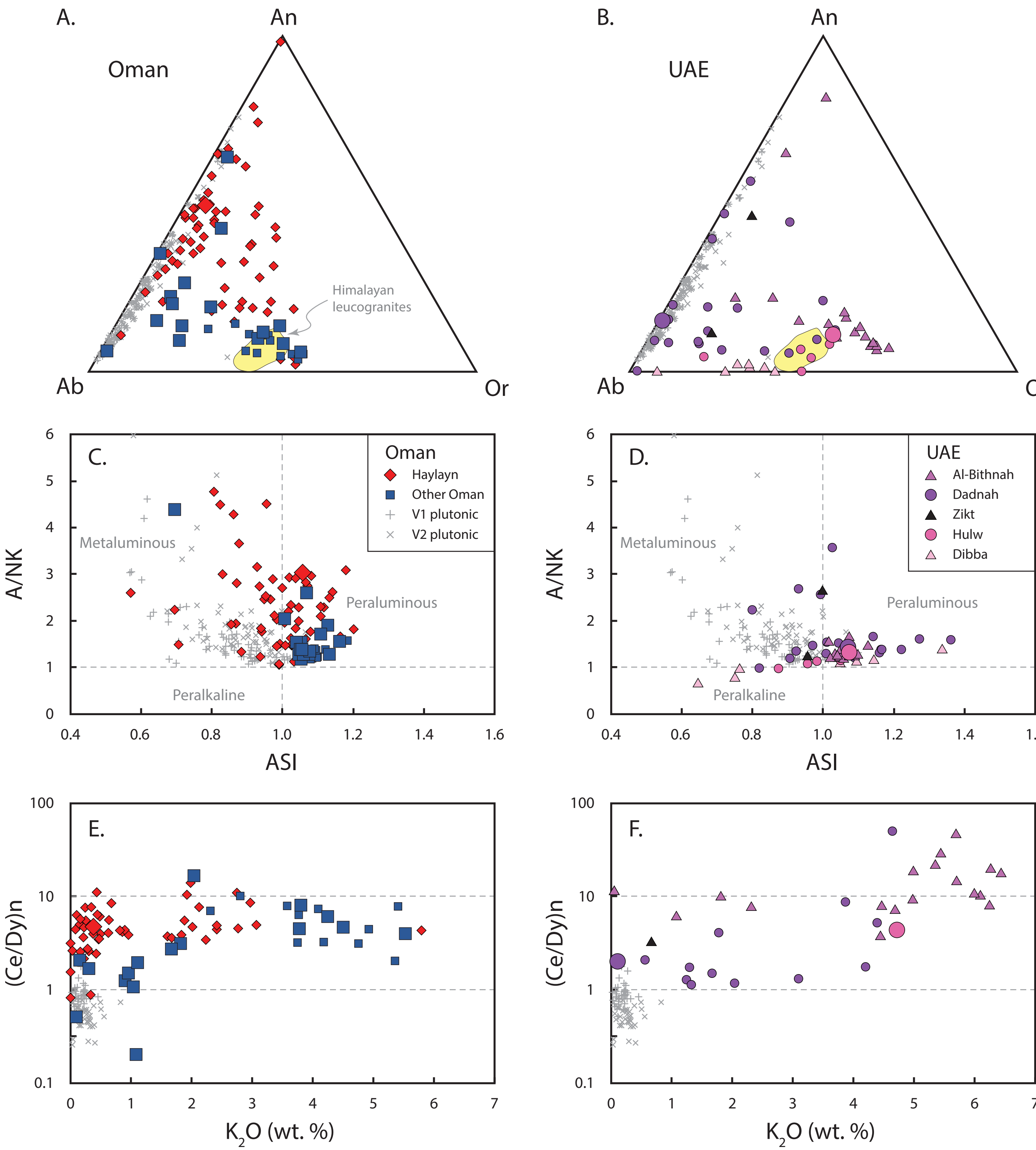

A.
Oman
An
Ab
Or
Himalayan leucogranites
B.
UAE
An
Ab
Or
C.
Oman
Haylayn
Other Oman
V1 plutonic
V2 plutonic
Metaluminous
Peraluminous
Peralkaline
A/NK
ASI
D.
UAE
Al-Bithnah
Dadnah
Zikt
Hulw
Dibba
Metaluminous
Peraluminous
Peralkaline
A/NK
ASI
E.
(Ce/Dy)n
K2O (wt. %)
F.
(Ce/Dy)n
K2O (wt. %)

Figure 2

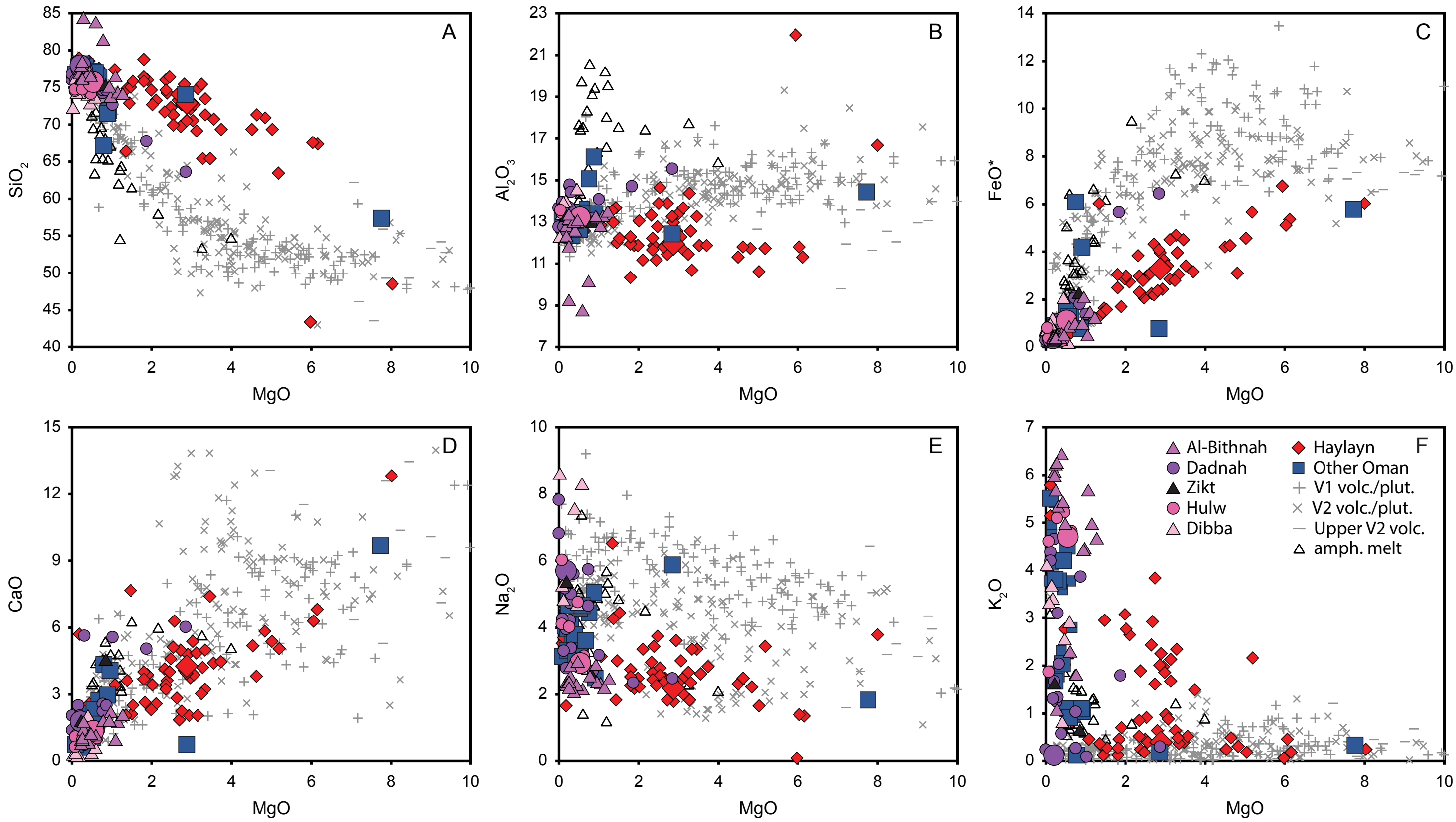
A
B
C
D
E
F
SiO2
Al2O3
FeO*
CaO
Na2O
K2O
MgO
Al-Bithnah
Dadnah
Zikt
Hulw
Dibba
Haylayn
Other Oman
V1 volc./plut.
V2 volc./plut.
Upper V2 volc.
amph. melt

Figure 3

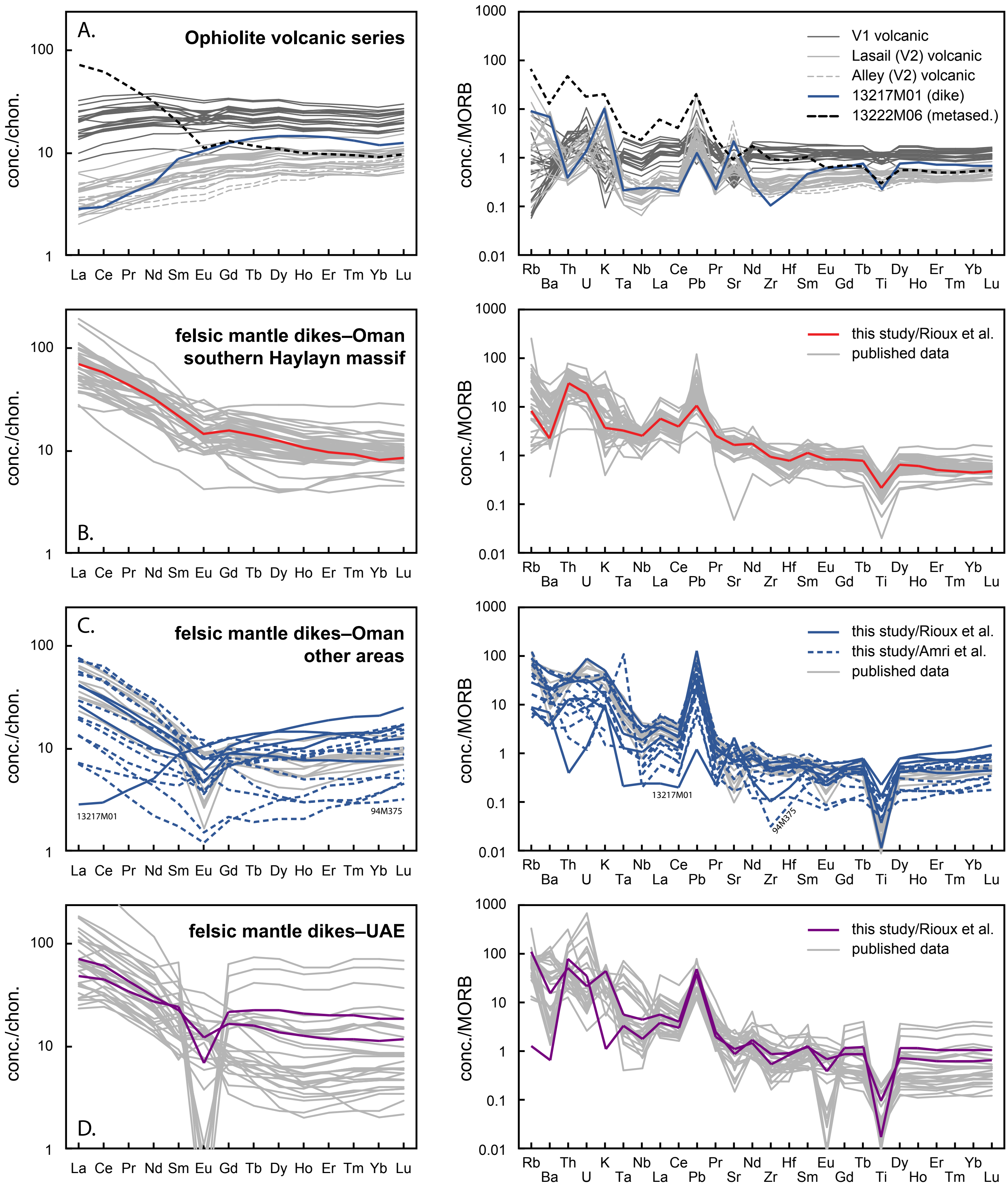

A.
Ophiolite volcanic series
B.
felsic mantle dikes–Oman southern Haylayn massif
C.
felsic mantle dikes–Oman other areas
D.
felsic mantle dikes–UAE
conc./chon.
conc./MORB
La Ce Pr Nd Sm Eu Gd Tb Dy Ho Er Tm Yb Lu
Rb Ba Th U K Ta Nb La Ce Pb Pr Sr Nd Zr Hf Sm Eu Gd Tb Ti Dy Ho Er Tm Yb Lu
1
10
100
1000
0.01
0.1
V1 volcanic
Lasail (V2) volcanic
Alley (V2) volcanic
13217M01 (dike)
13222M06 (metased.)
this study/Rioux et al.
published data
this study/Amri et al.
13217M01
94M375

Figure 4

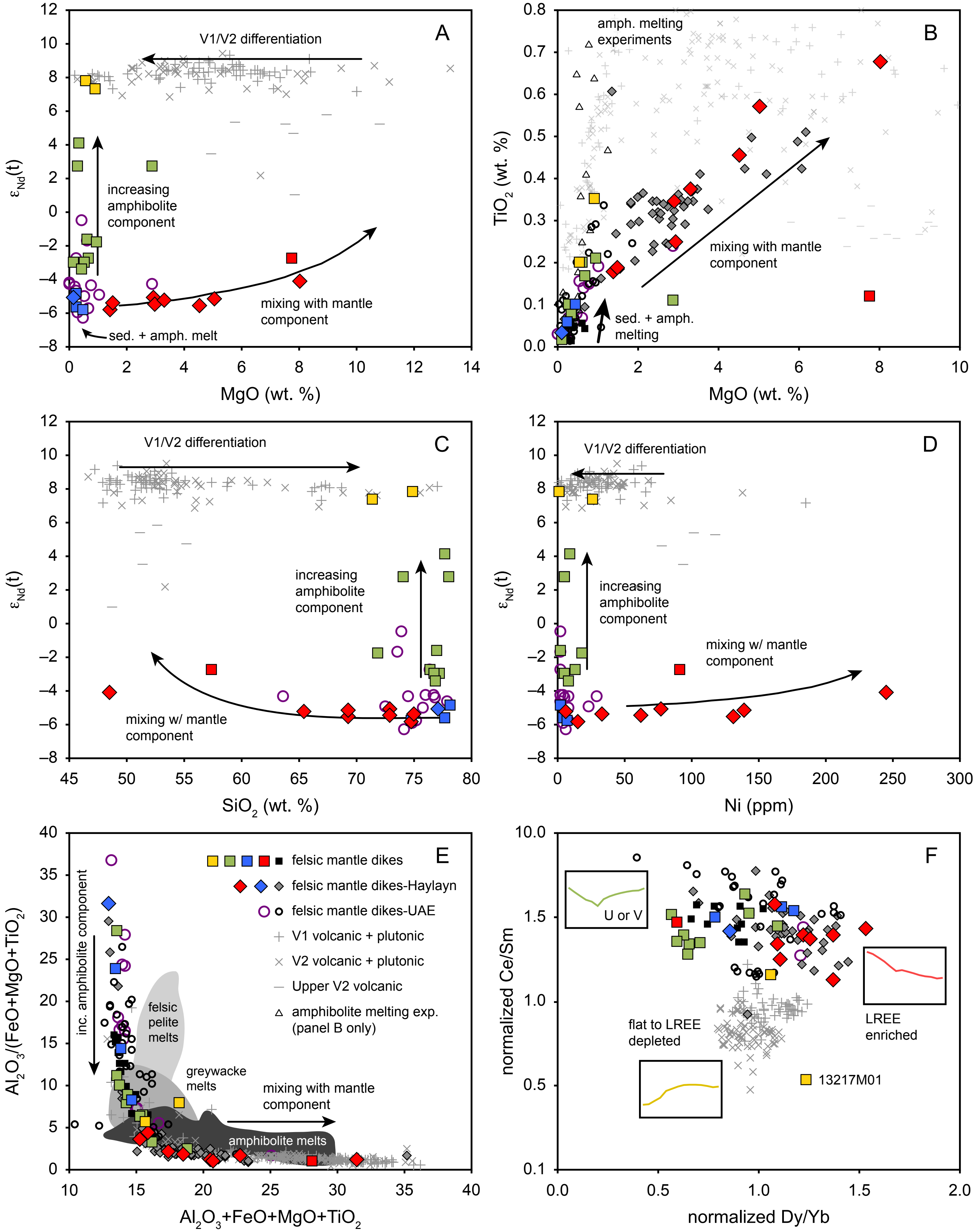

V1/V2 differentiation
A
increasing amphibolite component
mixing with mantle component
sed. + amph. melt
MgO (wt. %)
εNd(t)
amph. melting experiments
B
mixing with mantle component
sed. + amph. melting
TiO2 (wt. %)
MgO (wt. %)
V1/V2 differentiation
C
increasing amphibolite component
mixing w/ mantle component
SiO2 (wt. %)
εNd(t)
V1/V2 differentiation
D
increasing amphibolite component
mixing w/ mantle component
Ni (ppm)
εNd(t)
E
felsic mantle dikes
felsic mantle dikes-Haylayn
felsic mantle dikes-UAE
V1 volcanic + plutonic
V2 volcanic + plutonic
Upper V2 volcanic
amphibolite melting exp. (panel B only)
inc. amphibolite component
felsic pelite melts
greywacke melts
mixing with mantle component
amphibolite melts
Al2O3/(FeO+MgO+TiO2)
Al2O3+FeO+MgO+TiO2
F
U or V
LREE enriched
flat to LREE depleted
13217M01
normalized Ce/Sm
normalized Dy/Yb

Figure 5

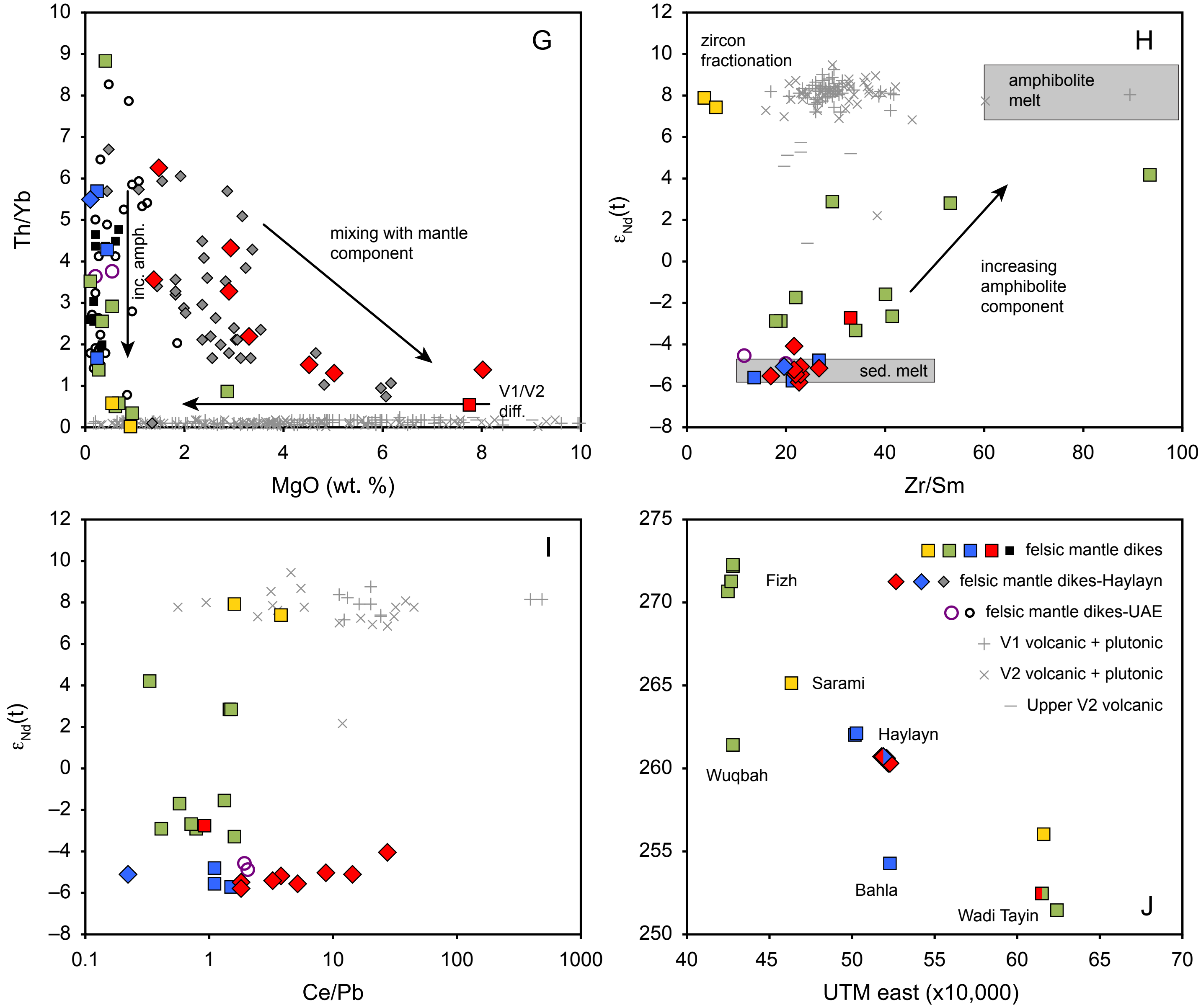

Figure 5 (cont.)

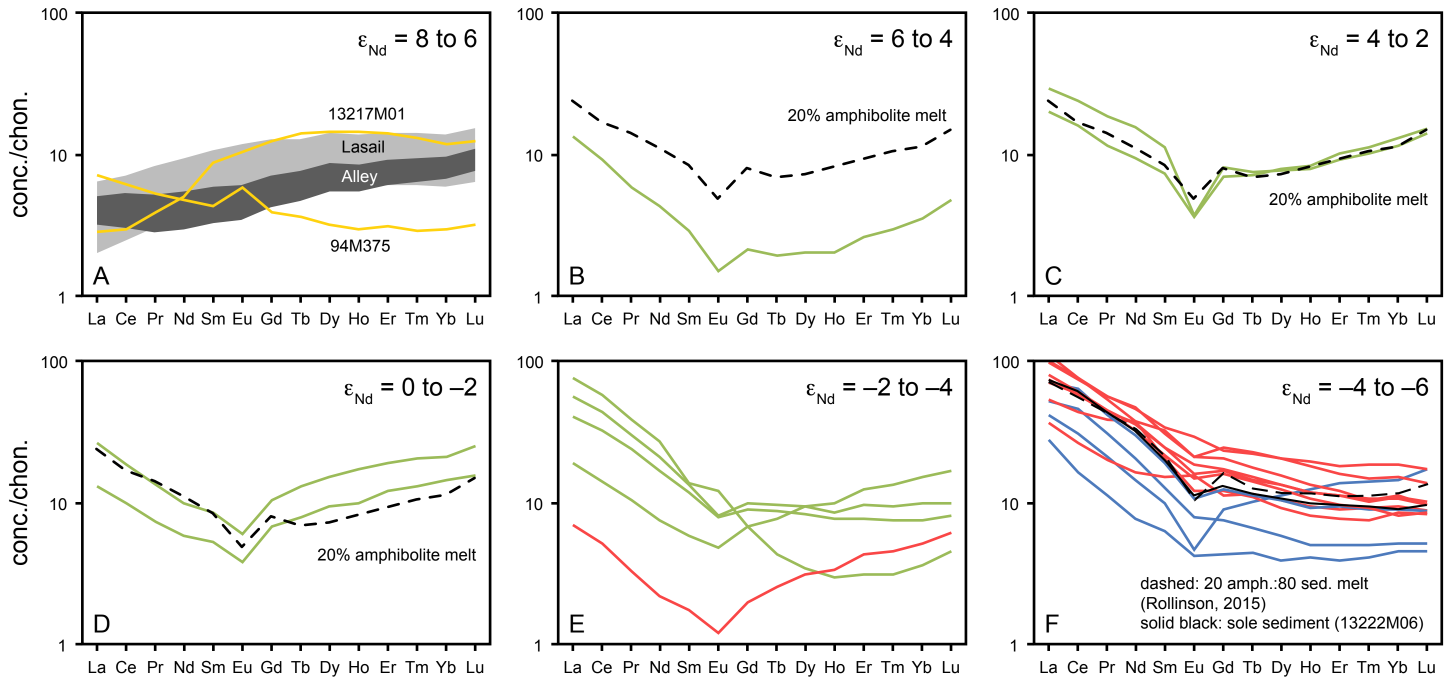

A
εNd = 8 to 6
13217M01
Lasail
Alley
94M375
B
εNd = 6 to 4
20% amphibolite melt
C
εNd = 4 to 2
20% amphibolite melt
D
εNd = 0 to –2
20% amphibolite melt
E
εNd = –2 to –4
F
εNd = –4 to –6
dashed: 20 amph.:80 sed. melt
(Rollinson, 2015)
solid black: sole sediment (13222M06)
conc./chon.
100
10
1
La Ce Pr Nd Sm Eu Gd Tb Dy Ho Er Tm Yb Lu

Figure 6

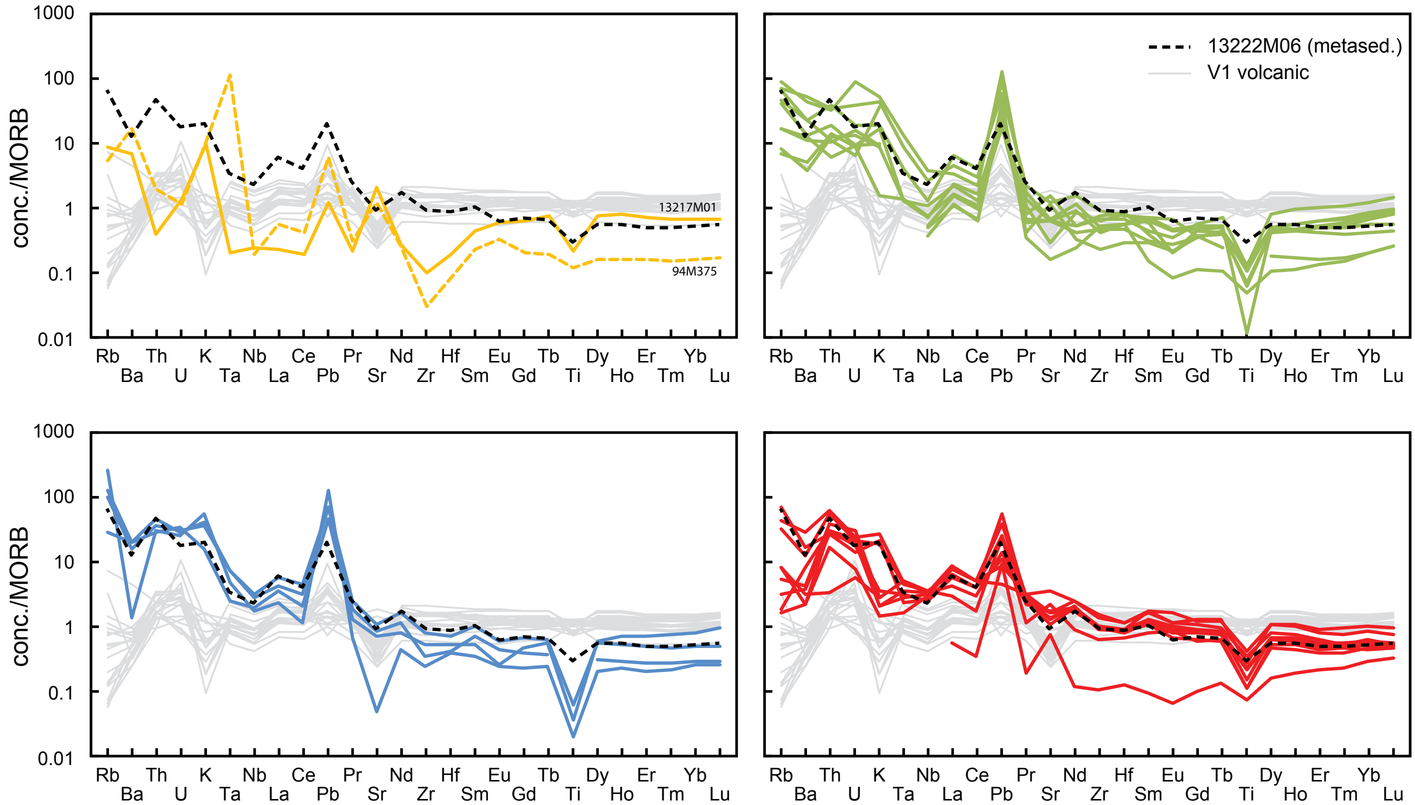

13222M06 (metased.)
V1 volcanic
conc./MORB
1000
100
10
1
0.1
0.01
13217M01
94M375
Rb Ba Th U K Ta Nb La Ce Pb Pr Sr Nd Zr Hf Sm Eu Gd Tb Ti Dy Ho Er Tm Yb Lu

Figure 7

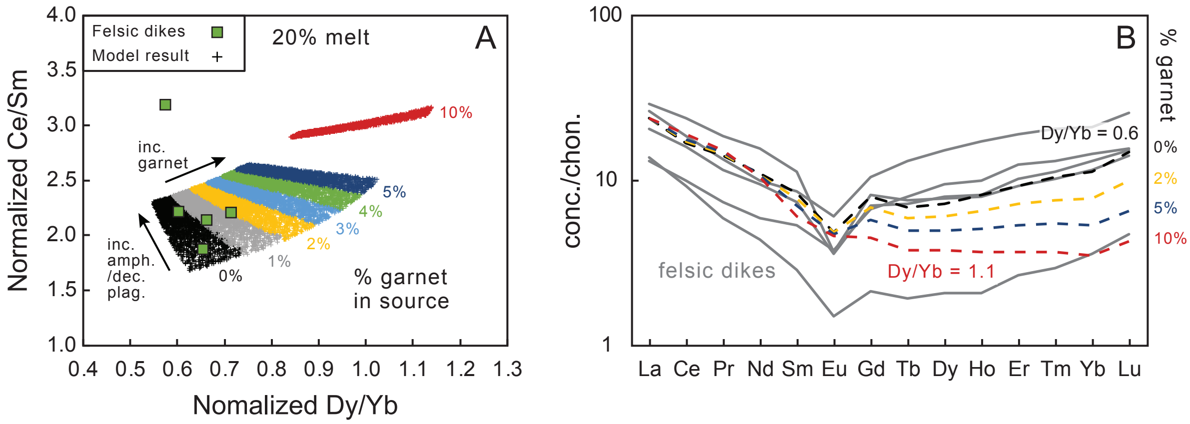
Felsic dikes
Model result
20% melt
A
Normalized Ce/Sm
Nomalized Dy/Yb
inc. garnet
inc. amph. /dec. plag.
% garnet in source
0%
1%
2%
3%
4%
5%
10%
B
% garnet
conc./chon.
Dy/Yb = 0.6
Dy/Yb = 1.1
felsic dikes
La Ce Pr Nd Sm Eu Gd Tb Dy Ho Er Tm Yb Lu

Figure 8

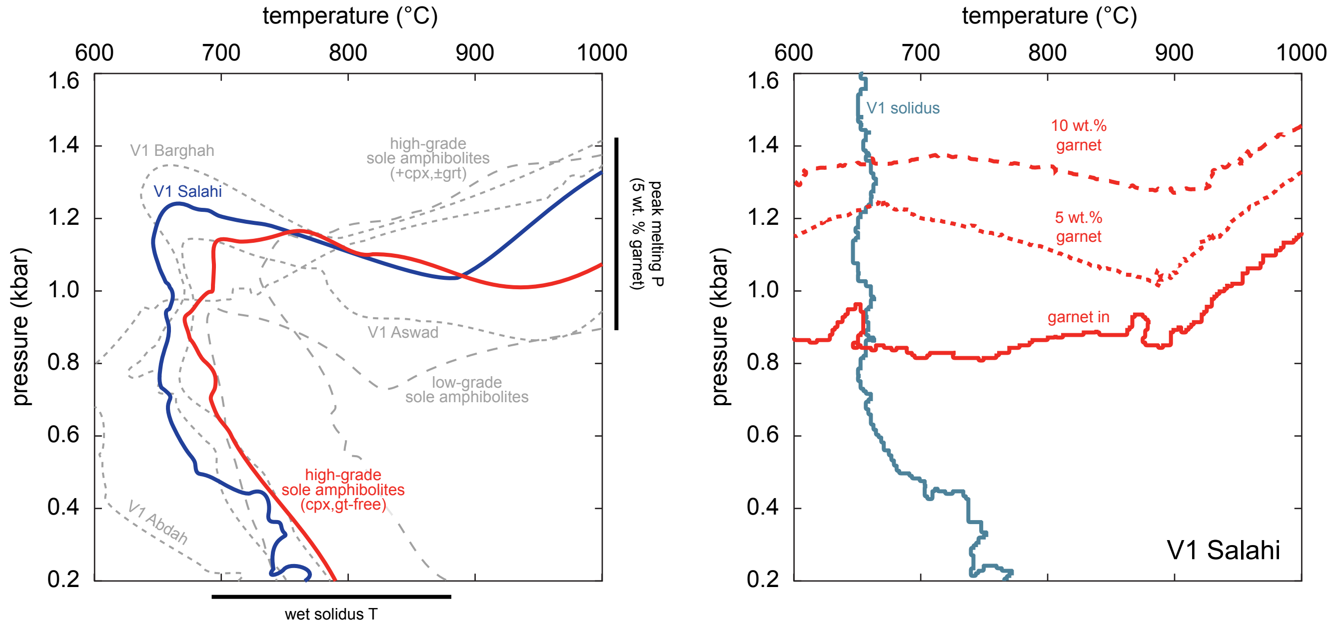
temperature (°C)
600
700
800
900
1000
1.6
1.4
1.2
1.0
0.8
0.6
0.4
0.2
pressure (kbar)
V1 Barghah
V1 Salahi
high-grade
sole amphibolites
(+cpx,±grt)
V1 Aswad
low-grade
sole amphibolites
high-grade
sole amphibolites
(cpx,gt-free)
V1 Abdah
wet solidus T
peak melting P
(5 wt. % garnet)
temperature (°C)
V1 solidus
10 wt.%
garnet
5 wt.%
garnet
garnet in
V1 Salahi

Figure 8

Journal of Geophysical Research

Supporting Information for

The origin of felsic intrusions within the mantle section of the Samail ophiolite: Geochemical evidence for three distinct differentiation trends

Matthew Rioux[1,2 *], Mathieu Benoit[3], Isma Amri[4], Georges Ceuleneer[3], Joshua Garber[5], Michael Searle[6], Kayla Leal[1]

[1] *Department of Earth Science, University of California, Santa Barbara, CA, 93106, USA*

[2] *Earth Research Institute, University of California, Santa Barbara, CA, 93106, USA*

[3] *Centre National de la Recherche Scientifique, Observatoire Midi-Pyrénées , 31400 Toulouse, France*

[4] *Faculté des Sciences, Département de Géologie, Université Abdelmalek Essaadi, Tétouan, Morocco.*

[5] *Department of Geosciences, The Pennsylvania State University, University Park, PA 16803, USA*

[6] *Department of Earth Sciences, University of Oxford, Oxford, OX1 3AN, UK*

[*] *corresponding author: rioux@eri.ucsb.edu*

Contents of this file

Text S1
Figures S1 to S8

Introduction

The supplemental material includes text describing tests of source composition and variable partition coefficients for the Monte Carlo trace element modeling and the details of the pseudosection modeling (Text S1); a figure detailing the data sources for the plots in the main paper (Figure S1); an extended trace element plot for the batch melting model (Figure S2); a figure detailing the impact of variable source compositions on the Monte Carlo batch partial melting models (Figure S3); a figuring showing the rare earth element patterns of the different source composition used in the Monte Carlo modeling (Figure S4); and four figures detailing the impact of variable garnet, amphibole, clinopyroxene and titanite partition coefficients on the Monte Carlo batch partial melting models (Figure S5–8).

Text S1.

Monte Carlo batch partial melting models

To critically assess our modeling results, we ran the Monte Carlo batch melting models using variable source compositions; 0–5 wt. % titanite; and variable amphibole, clinopyroxene, garnet, and titanite partition coefficients. For the source composition, we modeled melting of a range of V1 and sole compositions. For Figure 8 and Supplemental Figures S2 and S5–8 we used an average trace-element composition of V1 lavas compositions from Wadi Salahi [*Godard et al.*, 2006]. In Supplemental Figure S3, we show modeling results using the same parameters as Figure 8, with source compositions corresponding to the average V1 composition from the larger combined datasets of Godard et al. [2003; 2006] and a range of amphibolite compositions from the Green Pool locality in the Wadi Tayin massif, based on the data of Ishikawa et al. [2005] (Supplemental Figure S4). Ishikawa et al. [2005] argued that clinopyroxene in the high-grade amphibolites carries a metasomatic signature, and we therefore consider clinopyroxene-free amphibolites from the top 25 m below the Samail Thrust to be the best estimate of a sole protolith composition (Supplemental Figure S3c). For comparison, we also tested high grade clinopyroxene- (Supplemental Figure S3d) and garnet- (Supplemental Figure S3e) bearing compositions, as well as compositions from lower-grade amphibolites from >25 m below the thrust (Supplemental Figure S3f). The full range of tested source compositions have a minimal impact on the predicted maximum percentage garnet in the source; for all models, most of the dike trace-element data require <5 wt. % garnet, and the best fit models for all samples have 0–2 wt. % garnet. Using an average composition of V2 Lasail lavas permits 5–10 wt. % garnet in the source based solely on the Dy/Yb; however, the LREE depleted patterns of the V2 Lasail lavas lead to lower Ce/Sm than observed in the mantle dikes, making this an unlikely source composition.

Given that partition coefficients (Kd) can be sensitive to mineral composition, melt composition, *P,* and *T*, we further tested our models using a range of coefficients for amphibole, garnet, clinopyroxene and titanite. For garnet, we ran models using partition coefficients from natural and experimental studies in equilibrium with intermediate to felsic melts at 0.7–2.0 GPa and 800–1100ºC (Supplemental Figure S5) [*Klein et al.*, 2000; *Rubatto and Hermann*, 2007; *Sisson and Bacon*, 1992; *Taylor et al.*, 2015], including amphibolite melting experiments [*Qian and Hermann*, 2013]. The models are consistent with felsic dike generation by partial melting of an amphibolite source with ≤5 wt. % garnet, with the exception of Kd values derived from one experiment from Qian and Hermann [2013], two experiments from Klein et al. [2000], and one experiment from Rubatto and Hermann [2007], which permit ≥10 % garnet in the source for the higher Dy/Yb samples. These four outlying experiments have the lowest Kd values in the compiled dataset and a range of Kd_{Dy}/Kd_{Yb} (Supplemental Figure S5). Two factors suggest that the Kd values in these experiments are not appropriate for modeling the generation of the felsic mantle dikes: 1. The values from Qian and Hermann [2013] and Rubatto and Hermann [2007] are lower than other experiments from the same studies, and may be anomalous; and 2. Klein et al. [2000] and Rubatto and Hermann [2007] have shown that Kd_{REE} in garnet typically increase with decreasing *T*. Pseudosection modeling suggests that the amphibolite solidus temperatures were likely 700–800 ºC, below the temperatures in the outlying experiments (900–1100 ºC), and would therefore favor higher garnet-melt Kd_{REE}.

Amphibole favors the middle REE, with the distribution coefficients defining a convex-upward shape from La to Lu with an apex around Dy [*Sisson*, 1994]. However, amphibole-melt partitioning varies with melt composition, such that the REE are more compatible and there is greater fractionation between the MREE and HREE in more felsic melts [*Sisson*, 1994]. To test the sensitivity of our models to the amphibole partition coefficients, we used a range of experimentally and naturally derived values in equilibrium with mafic to felsic melts at 0.2–5 GPa and 800–1100 ºC (Supplemental Figure 6) [*Adam and Green*, 1994; *Adam et al.*, 1993; *Brenan et al.*, 1995; *Dalpé and Baker*, 2000; *Hilyard et al.*, 2000; *Klein et al.*, 1997; *LaTourrette et al.*, 1995; *Qian and Hermann*, 2013; *Sisson*, 1994; *Tiepolo et al.*, 2007; *Tiepolo et al.*, 2000]. The partition coefficients for felsic melts from Sisson [1994] best reproduce the observed U- to V-shape of the dikes (low Dy/Yb). All other partition coefficients yield flatter HREE (lower Dy/Yb) than observed, indicating that the low modal percent garnet predicted by our melting models is not a result of the selected amphibolite partition coefficient (i.e., any other amphibole partition coefficients require an even lower percent garnet). Clinopyroxene can similarly favor the MREE [*Bédard*, 2014]—especially for more felsic melt compositions [e.g., *Sisson*, 1991]—however, using even the most extreme clinopyroxene partition coefficients still suggests <5 wt. % garnet in the source of the felsic mantle dikes (Supplemental Figure 7).

The fact that many of the existing amphibole partition coefficients predict higher Dy/Yb than observed in the amphibolite-rich felsic mantle dikes raises the possibility that another phase is contributing to or controlling the U- to V-shaped REE patterns. A likely candidate is titanite, which has an affinity for the MREE and is abundant in some amphibolites (up to ~1 wt. %) from the metamorphic sole of the ophiolite. To test the potential role of titanite, we ran models using both our preferred amphibole partition coefficients [*Rollinson*, 2015; *Sisson*, 1994] and amphibole partition coefficients from the amphibolite melting experiments of Qian and Hermann [2013], which predict higher Dy/Yb. We used 0–5 wt. % titanite and tested the range of titanite partition coefficients from Tiepolo et al. [2002], Bachmann et al. [2005], Prowatke and Klemme [2005], and Olin and Wolff [2012] (Supplemental Figure S8). The Prowatke and Klemme [2005] partition coefficients for Dy and Yb are based on interpolation using Onuma diagrams, limiting the accuracy of these values. Incorporation of 0–5 wt. % titanite had little impact on the predicted melt Dy/Yb for most experimentally determined titanite partition coefficients. The exceptions were models using partition coefficient from the high alumina saturation index experiments (ASI260, ASI280) of Prowatke and Klemme [2005] and measured values from the Fish Canyon Tuff from Bachmann et al. [2005]. Melting models with these partition coefficients did impact the Dy/Yb, but also led to steeper LREE slopes than observed in most mantle dikes, and the best fit models still contain <5 wt. % garnet in the source. Overall, our models using currently available titanite partition coefficients suggest that the U-shaped REE are primarily driven by amphibole (and/or clinopyroxene) in the source and affirm that the REE patterns of the felsic mantle dikes are most consistent with <5 wt. % garnet in the source. While titanite does not appear to be the primary control on the Dy/Yb of the melt, it is possible it plays a role in producing the V- versus U-shape for the REE; additional titanite partitioning data are need at the appropriate *P, T,* and titanite and whole rock compositions to better understand the relative partitioning of middle REE relative to amphibole. If the higher Ce/Sm values (i.e. steeper LREE) predicted using the Bachmann et al. [2005] and high ASI Prowatke and Klemme [2005] titanite partition coefficients are accurate, the inclusion of titanite in the source could explain the elevated Ce/Sm of one of the dike samples.

Pseudosection modeling

For all calculations, we used the Holland and Powell [2011] thermodynamic dataset, with H_2O modeled using the CORK model of Holland and Powell [1991]. Thermodynamic modelling was performed in the system SiO_2-TiO_2-Al_2O_3-FeO-Fe_2O_3-MnO-MgO-CaO-Na_2O-K_2O-H_2O. Fe^{3+} was cast as 25% of total Fe, but minor variations in this value do not significantly affect the calculated results. Prior to calculating P-T pseudosections, we calculated T-X(H_2O) sections at P = 1.0 GPa for each bulk composition, and adopted the amount of water necessary to achieve H_2O

saturation at the solidus for all P-T calculations. Hydrated conditions during initial melting are consistent with the tectonic setting of metamorphic sole formation [Rioux et al., 2016; Searle and Cox, 2002a], as well as observations from non-mafic sole lithologies (Garber et al., 2020). Solution models were sourced from Green et al. [2016] for tonalitic melt, augite, and clinoamphibole; White et al. [2014a; 2014b] for garnet, chlorite, biotite, white mica, cordierite, orthopyroxene and ilmenite; Holland and Powell [2011] for epidote; Fuhrman and Lindsley [1988] for feldspar; and White et al. [2002] for spinel. All pseudosections were run from 2–16 kbar and 600–1000 °C.

Cited references are provided in the main text.

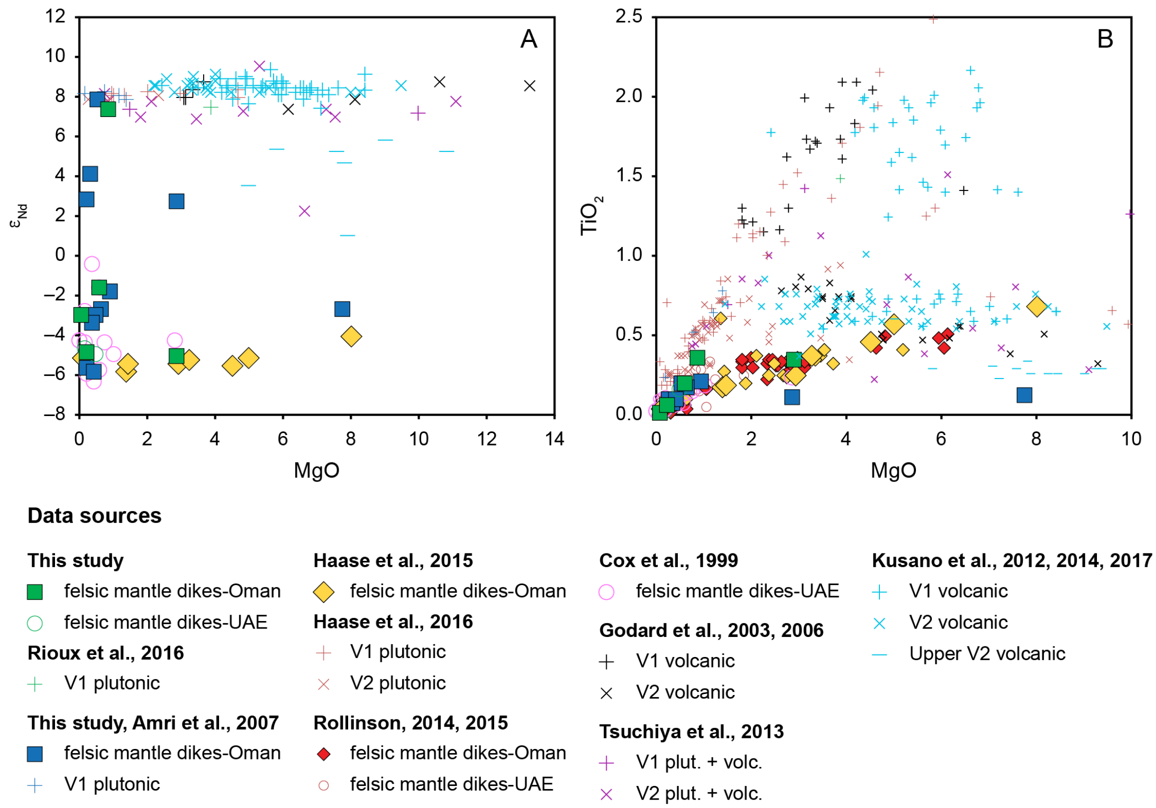

Figure S1. Data sources used in the compilation figures for this study (Figures 3 and 5). For data from felsic mantle dikes, the larger plot symbols correspond to samples with Nd isotopic data. Note that the Y-axis scale for (b) is larger than the scale for Figure 5d. The following data plot off scale in Figure 5: (a, d) High TiO_2 and MgO data for the V1 and V2 series; (e–g) anomalous points from the UAE mantle dikes; (i) a single anomalous V1 datum.

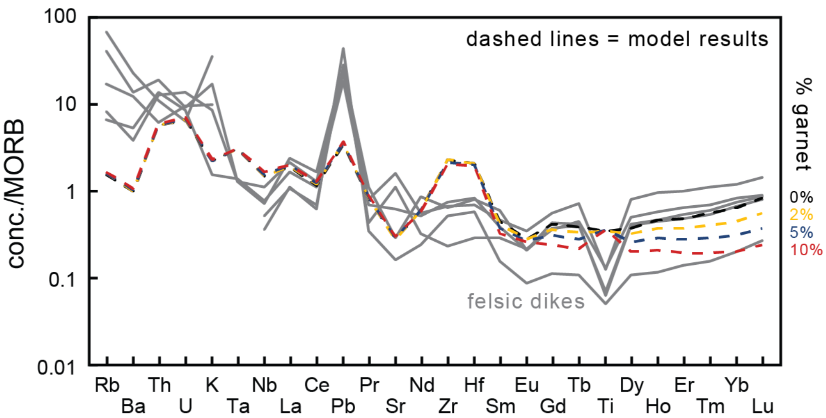

Figure S2. Extended trace element plot for the model shown in Figure 8b. Gray lines correspond to felsic mantle dikes with $\varepsilon_{Nd}(t) > -2$ and the dashed lines are the model results, with 0–10 wt. % garnet. The plotted trace element patterns are for 20% batch modal melting of an amphibolite source with ~25 wt. % amphibole, ~60 wt. % plagioclase, and 15 wt. % clinopyroxene. Data are normalized to normal mid-ocean ridge basalt [*Hofmann*, 1988].

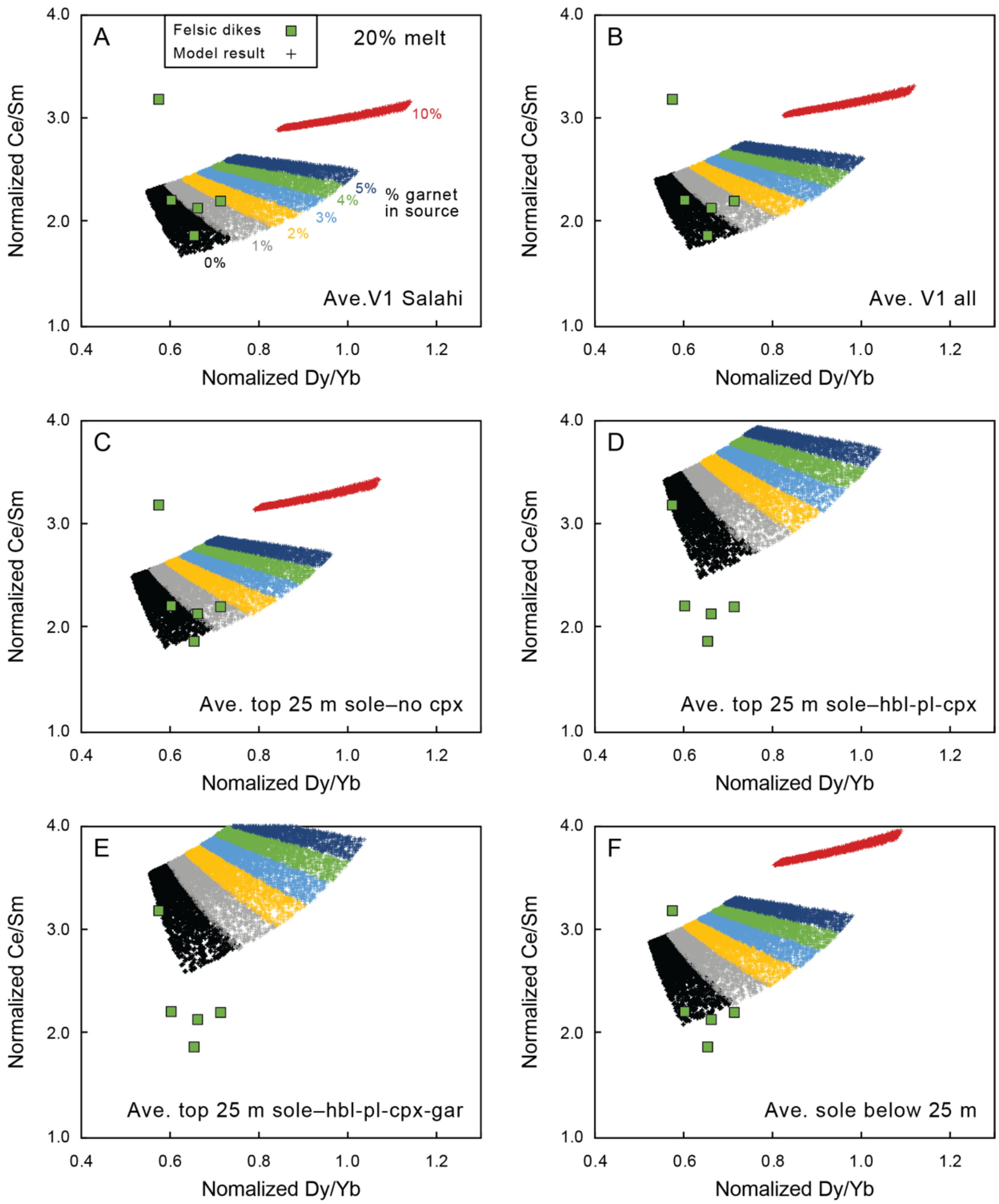

Figure S3. Monte Carlo modal batch melting models using different source compositions. All other parameters are the same as in Figure 8 in the main text—models have no titanite in the source. The modeled source compositions are as follows: (a) Average of V1 lava compositions from Wadi Salahi [*Godard et al.*, 2006]. This is the source composition used in Figures 8, S2, and S4–6. (b) Average of all V1 lavas from Godard et al. [2003; 2006]. (c) Average cpx-free sole amphibolites from the top 25 below the Samail Thrust. (d) Average cpx+plag+hbl amphibolites from the top 25 m. (e) Average cpx+plag+hbl+gar amphibolites from the top 25 m. (f) Average sole amphibolites from below 25 m. All sole amphibolite compositions are from the Green pool sole exposure in the Wadi Tayin massif [*Ishikawa et al.*, 2005].

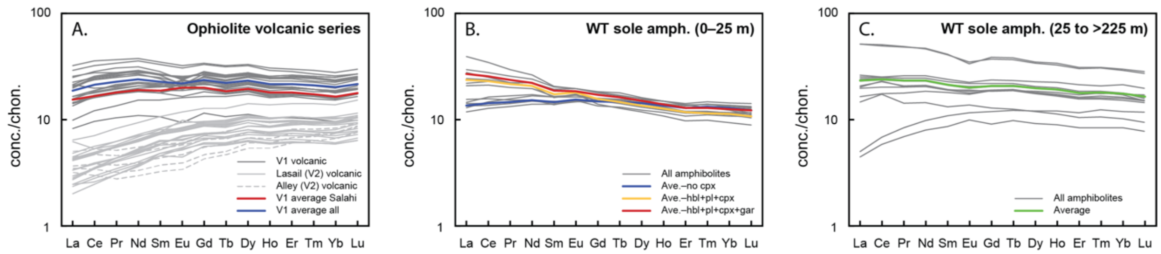

Figure S4. Rare earth element patterns for the source compositions modeled in the main text and Supplemental Figure S3. V1 compositions are from Godard et al. [2003; 2006] and amphibolite compositions are from Ishikawa et al. [2005].

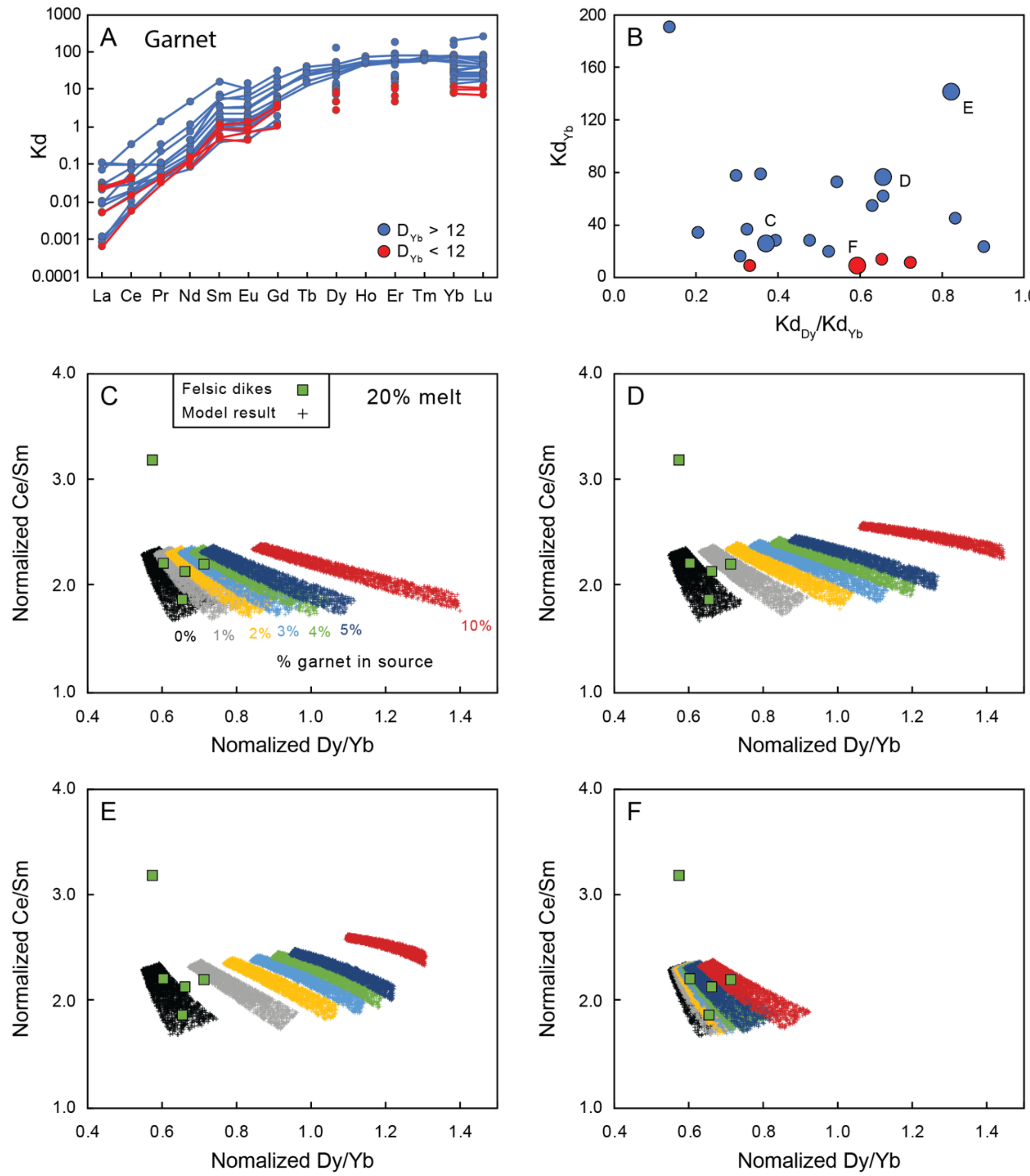

Figure S5. Variability of garnet partition coefficients in equilibrium with intermediate to felsic melts. (a–b) Published garnet distribution coefficients from experimental and natural data [*Klein et al.*, 2000; *Qian and Hermann*, 2013; *Rubatto and Hermann*, 2007; *Sisson and Bacon*, 1992; *Taylor et al.*, 2015]. Red data points are the four experiments with the lowest Kd values, discussed in the text. Larger, labeled symbols in (b) correspond to garnet partition coefficients used in (c–f). (c-f) Monte Carlo modal batch melting models using variable garnet partition coefficients. All other parameters are the same as in Figure 8 in the main text. Partition coefficients in (c–f) are from Klein et al. [c, f; 2000], Taylor et al. [d; 2015], and Sisson and Bacon [e; 1992].

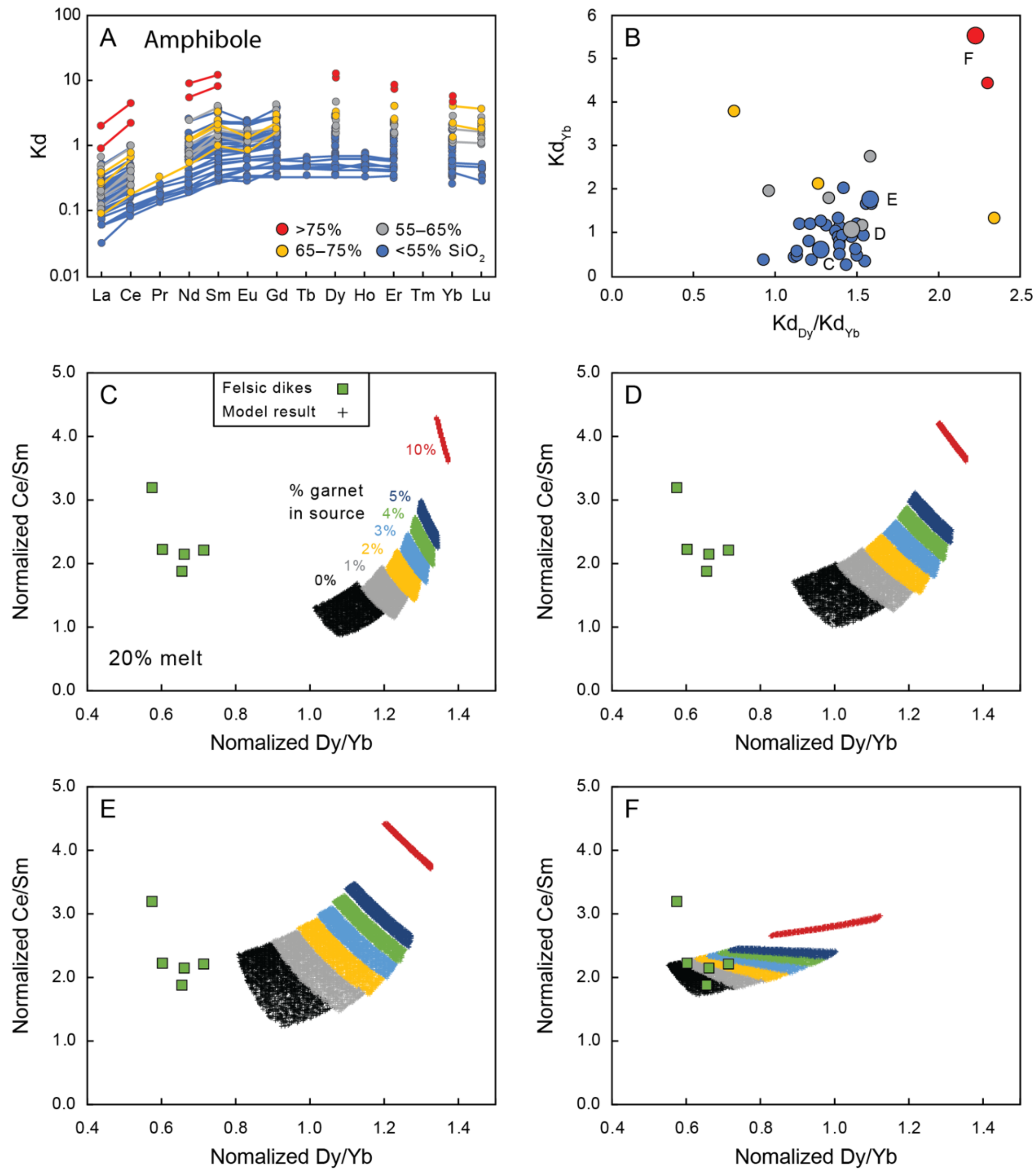

Figure S6. Variability of amphibole partition coefficients. (a–b) Published amphibole distribution coefficients from experimental and natural data [*Adam and Green*, 1994; *Adam et al.*, 1993; *Brenan et al.*, 1995; *Dalpé and Baker*, 2000; *Hilyard et al.*, 2000; *Klein et al.*, 1997; *LaTourrette et al.*, 1995; *Qian and Hermann*, 2013; *Sisson*, 1994; *Tiepolo et al.*, 2007; *Tiepolo et al.*, 2000]. Data are divided by the SiO_2 content of the equilibrium melt. Larger, labeled symbols in (b) correspond to amphibole partition coefficients used in (c–f). (c-f) Monte Carlo modal batch melting models using variable amphibole partition coefficients. All other parameters are the same as in Figure 8 in the main text. Partition coefficients in (c–f) are from Tiepolo et al. [c, e; 2000] and Sisson [d, f; 1994].

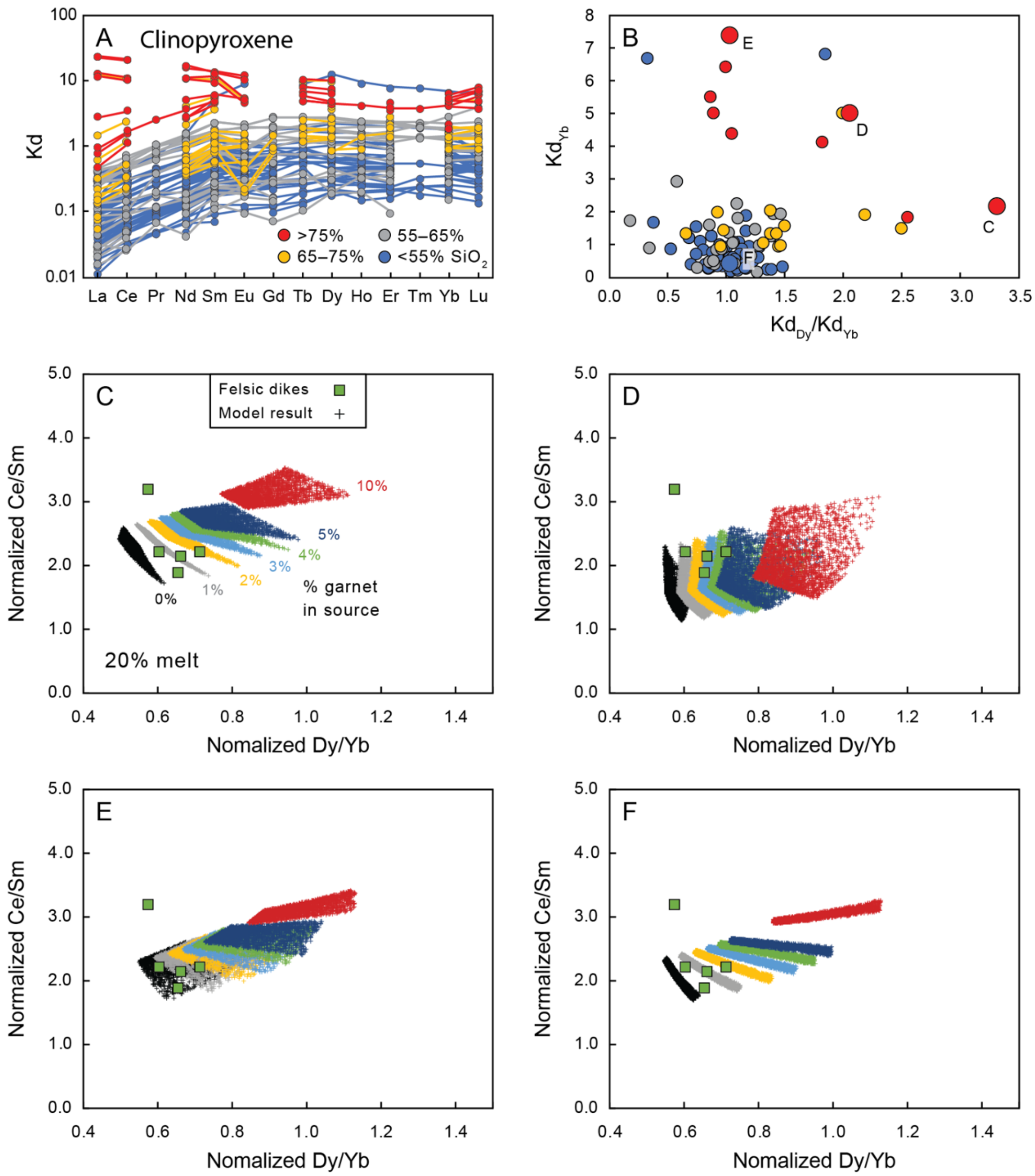

Figure S7. Variability of clinopyroxene partition coefficients. (a–b) Published clinopyroxene distribution coefficients from experimental and natural data [values from the compilation of *Bédard*, 2014]. Data are divided by the SiO_2 content of the equilibrium melt. Larger, labeled symbols in (b) correspond to clinopyroxene partition coefficients used in (c–f). (c-f) Monte Carlo modal batch melting models using variable clinopyroxene partition coefficients. All other parameters are the same as in Figure 8 in the main text. Partition coefficients in (c–f) are from Sisson [1991], Mahood and Hildreth [1983], Olin and Wolff [2010] and Norman et al. [2005], respectively.

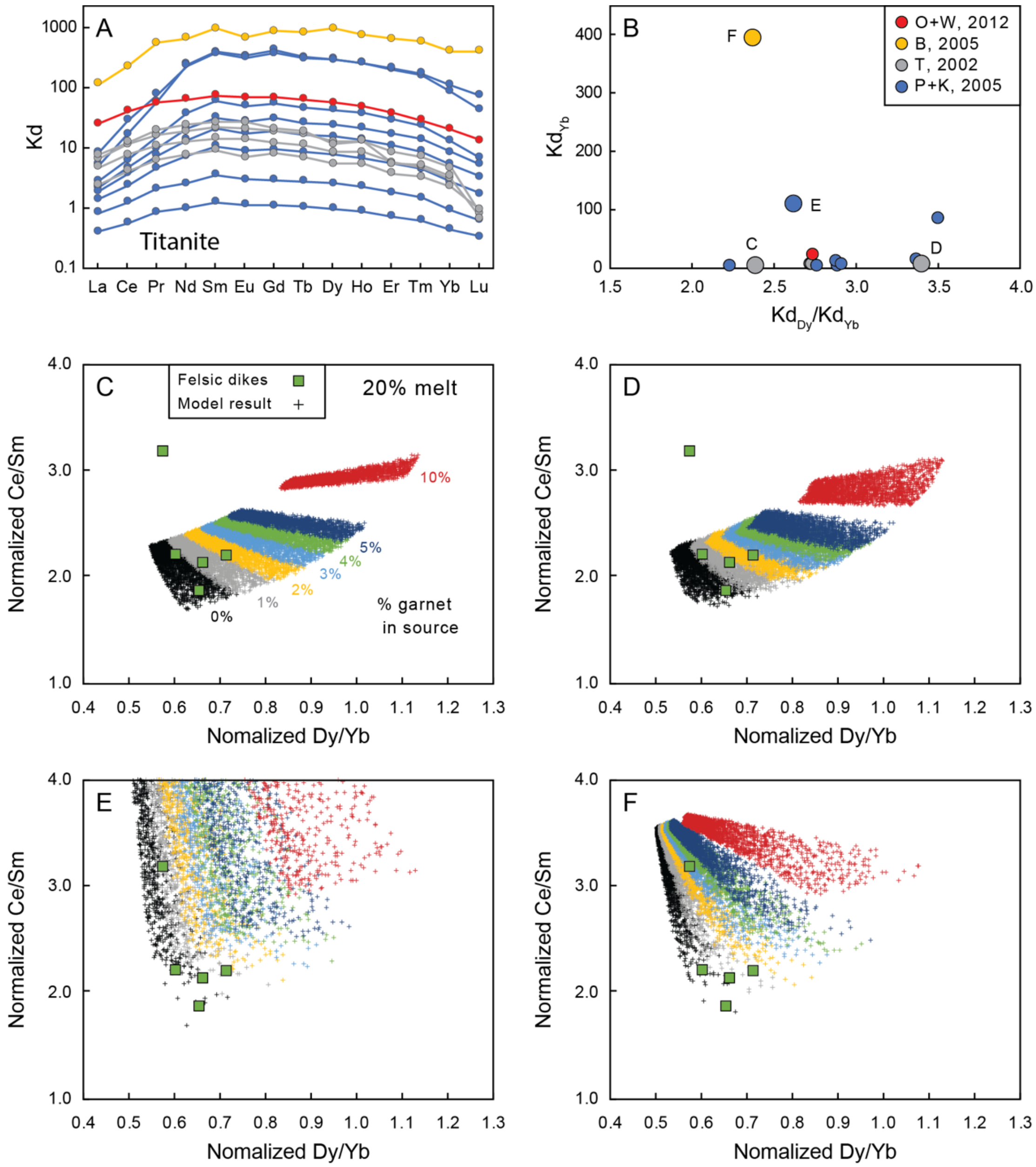

Figure S8. Variability of titanite partition coefficients. (a–b) Published titanite distribution coefficients from experimental and natural data [*Bachmann et al.*, 2005; *Olin and Wolff*, 2012; *Prowatke and Klemme*, 2005; *Tiepolo et al.*, 2002]. Data are divided by study. Larger, labeled symbols in (b) correspond to titanite partition coefficients used in (c–f). (c-f) Monte Carlo modal batch melting models using variable titanite partition coefficients. Modal titanite varies from 0–5 wt. %; all other parameters are the same as in Figure 8 in the main text. Partition coefficients in (c–f) are from Tiepolo et al. [c, d; 2002], Prowatke and Klemme [e; 2005], and Bachmann et al. [f; 2005].